

1

2

3

4

For positioning electrodes in the ATLAS experiment's New Small Wheels using detector characterization techniques

5

Lia Formenti

6

7

8

Department of Physics
McGill University, Montreal
October, 2021

9

10

11

12

13

A thesis submitted to
McGill University
in partial fulfillment of the
requirements of the degree of
Master of Science

¹⁵ Table of Contents

¹⁶ 1	Introduction	1
¹⁷ 2	High energy particle physics at the LHC and the ATLAS experiment	4
¹⁸ 2.1	The Standard Model	4
¹⁹ 2.2	Beyond the Standard Model	6
²⁰ 2.3	Studying high energy particle physics with accelerators	7
²¹ 2.4	The Large Hadron Collider	9
²² 2.5	Luminosity	9
²³ 2.6	The High-luminosity LHC	10
²⁴ 2.7	The ATLAS experiment	10
²⁵ 3	The New Small Wheels	17
²⁶ 3.1	Motivation for the New Small Wheels (NSWs)	17
²⁷ 3.2	Design of the NSWs	19
²⁸ 3.3	Small-strip thin gap chambers	21
²⁹ 3.4	sTGC Quadruplet Construction	22
³⁰ 3.5	NSW alignment	25
³¹ 4	Using cosmic muons to measure relative strip position offsets	28
³² 4.1	Cosmic rays	28
³³ 4.2	Experimental setup	29

34	4.3 Data acquisition	30
35	4.4 Data preparation	30
36	4.4.1 Cuts on electrode hits	30
37	4.4.2 Clustering and tracking	31
38	4.5 Measuring relative local offsets	33
39	4.6 Visualizing relative alignment between layers	36
40	4.7 Systematic uncertainty	38
41	4.8 Discussion	40
42	5 Using x-rays to measure relative strip position offsets	41
43	5.1 Experimental setup	41
44	5.2 Data acquisition	43
45	5.3 Data preparation	43
46	5.4 Measuring local offsets	43
47	5.5 Measuring relative local offsets	45
48	6 Comparing cosmic muon and x-ray relative strip position offsets	49
49	6.1 Assessing correlation	49
50	6.2 Discussion	54
51	7 Outlook and summary	56
52	7.1 Outlook	56
53	7.2 Summary	57
54	References	58
55	APPENDICES	65
56	A Cluster position uncertainty	66
57	A.1 Cluster definition	66
58	A.2 Effect of fit algorithm on cluster mean	66
59	A.3 Effect of uncertainty in cluster mean on track residuals	67

60	B Analysis statistics	68
61	C Analysis systematics	70
62	C.1 Residual distribution fit function	70
63	C.2 Cosmic muon data collection voltage	71
64	C.3 Cluster fit algorithm	73
65	C.4 Differential non-linearity	74
66	D Printable plots	77

Abstract

68 The particle collision rate at the Large Hadron Collider (LHC) will be increased up to
69 seven times its design value in 2025-2027 by an extensive upgrade program. The innermost
70 endcaps of the ATLAS muon spectrometer consist of two wheels of muon detectors that must
71 be replaced to maintain the muon momentum resolution in the high-rate environment. The
72 so-called New Small Wheels (NSWs) are covered with two detector technologies: micromegas
73 and small-strip thin gap chambers (sTGCs). sTGCs are gas ionization chambers that hold a
74 thin volume of gas between two cathode boards. One board is segmented into strips of 3.2 mm
75 pitch that are used to precisely reconstruct the coordinate of a passing muon. Modules of
76 four sTGCs glued together into quadruplets cover the NSWs. Quadruplets were designed
77 to achieve 1 mrad angular resolution to fulfill the spectrometer's triggering and precision
78 tracking requirements. To deliver the angular resolution the strips must be positioned in the
79 ATLAS coordinate system to within the chambers' position resolution (less than 100 μm).
80 So, the internal geometry of the quadruplets must be characterized. At McGill University,
81 quadruplets were characterized using a cosmic ray hodoscope before being sent to CERN,
82 where the charge profile left by x-rays is used to measure the offset of the strip patterns
83 at known positions on the quadruplet surface. The x-ray measurements are being used to
84 position the strips within the ATLAS alignment system. They have acceptable but limited
85 precision and do not span the whole area of the strip layers. Given the importance of
86 alignment, the x-ray method must be validated by an independent method. Cosmic ray data
87 is used to characterize the relative alignment between layers and validate the x-ray method.

Résumé

89 Le rythme des collisions du collisionneur LHC augmentera jusqu'à sept fois le rythme nominal
90 en 2025-2027 par un programme d'amélioration majeur et varié. Une partie du spectromètre
91 à muons est composée de deux roues couvertes de détecteurs de muons qu'il faut remplacer
92 pour maintenir la résolution d'élan après l'augmentation du rythme. Appelées les nouvelles
93 petites roues (NSWs), elles sont couvertes de deux technologies: des chambres micromegas
94 et des chambres sTGCs (chambres à petites bandes et à intervalles fins). Les sTGCs sont
95 des chambres d'ionisation de gaz, qui contiennent un volume de gaz fin entre deux panneaux
96 cathodiques. Un panneau est segmenté à petites bandes avec une pente de 3.2 mm qui
97 est utilisé pour reconstruire précisément la coordonnée d'un muon qui passe. Des modules
98 de quatres sTGCs collées ensembles en quaduplets couvrent les NSWs. Les quaduplets
99 étaient conçus pour réaliser une résolution angulaire de 1 mrad pour satisfaire les besoins des
100 systèmes de déclenchement et de mesures de précision. Pour réaliser la résolution angulaire
101 il faut que les bandes soient positionées dans ATLAS avec une précision à moins de 100 μm ,
102 la résolution de position des sTGCs. Alors, il faut caractériser la géométrie internes des
103 quaduplets. À l'Université de McGill, les quaduplets étaient caractériser avec des rayons
104 cosmiques avant les envoyer à CERN, où le profil de charge laisser par des rayons-X est utilisé
105 pour mesurer le déplacement du motif des bandes à des positions spécifiques sur la surface
106 des quaduplets. Les déplacements mesurer pas les rayons-X sont utilisés pour positionner
107 les bandes dedans le système d'alignement d'ATLAS. Ils ont une précision acceptable mais
108 limitée, et ne couvrent pas la région entière des panneaux. Étant donné l'importance de
109 l'alignement, il faut une méthode indépendante pour valider la méthode des rayons-X. Les
110 données recueillies avec les rayons cosmiques sont utilisées pour charactariser l'alignement
111 relatif entre les panneaux et pour valider la méthode des rayons-X.

Acknowledgements

- 113 Experimental particle physics projects are never done alone. I am grateful to have been
114 working with the ATLAS Collaboration for two years now.
- 115 Thank you to Dr. Brigitte Vachon for her guidance throughout this project and for editing
116 this thesis. I am consistently amazed by her ability to jump into the details of my project
117 and discuss them with me.
- 118 Thanks also to Dr. Benoit Lefebvre, who collected some of the data used in this thesis, wrote
119 several software tools I used to analyze the data and advised me several times throughout
120 this project.
- 121 Thank you to my labmates at McGill University, Dr. Tony Kwan, Kathrin Brunner, John
122 McGowan and Charlie Chen. Kathrin taught me mechanical skills that I will apply elsewhere.
123 Tony, manager of the laboratory, created the most encouraging, trusting and productive work
124 environment I have ever been apart of.
- 125 Thank you to the friends I can call on at anytime, and thank you to my family whose
126 constant support makes every step possible.

Contribution of authors

I, the author, was involved in collecting the cosmic ray data from September 2019 - March 2021. I did not design the cosmic ray testing procedure nor write the data preparation software, but I participated in using the software to analyze cosmic ray results. In the thesis, the terms “clustering,” “local offset” and “relative local offset” are defined. Cosmic ray clustering was done in the data preparation software, but I redid the fit afterwards to explore sensitivity to the fit algorithm. With help from Dr. Lefebvre and Dr. Vachon, I helped design the software that calculated the relative local offsets from cosmic ray data. I wrote that software on my own. I was not involved in the design, data collection, data preparation or analysis of the x-ray data. I used the x-ray local offsets calculated using x-ray data analysis software to calculate relative local offsets with x-rays. I did the comparison between the x-ray and cosmic ray data.

I hereby declare that I am the sole author of this thesis. This is a true copy of the thesis, including any required final revisions, as accepted by my examiners.

¹⁴¹ Chapter 1

¹⁴² Introduction

¹⁴³ High energy particle physics seeks to explain the existence of a set of fundamental particles
¹⁴⁴ whose interactions determined the evolution of the universe. The set and their interactions
¹⁴⁵ are described shockingly well by the Standard Model (SM) of particle physics; however, the
¹⁴⁶ questions the SM does not address motivate more experimentation.

¹⁴⁷ Accelerators collide particles to generate interactions that can be captured by detectors and
¹⁴⁸ subsequently studied. The Large Hadron Collider (LHC) [1] at CERN will remain the world's
¹⁴⁹ most energetic particle accelerator for at least the next decade [2], making it an indispensable
¹⁵⁰ tool for studying interactions in an environment as close as can be simulated to the early
¹⁵¹ universe. The ATLAS experiment [3] is one of the LHC's general-purpose particle detector
¹⁵² arrays, used to detect the products of LHC collisions. A feat of engineering, every detail
¹⁵³ matters. This work showcases one example of how precise positioning of electrodes in particle
¹⁵⁴ detectors is necessary to study the interactions of particles in high-energy collisions.

¹⁵⁵ The High-Luminosity Large Hadron Collider (HL-LHC) project [2] was approved to combat
¹⁵⁶ the plateau in statistical gain of recording particle collisions at the LHC. Being the most
¹⁵⁷ energetic particle accelerator, the LHC still offers unique physics opportunities for studying
¹⁵⁸ the Higgs and electroweak sectors of the SM [4]; if study at the energy frontier is to continue,
¹⁵⁹ the LHC must go on. The HL-LHC upgrade aims to increase the luminosity of the LHC by
¹⁶⁰ up to a factor of 7 in the next 10 years, which ultimately increases the number of meaningful
¹⁶¹ collisions. Naturally, various sub-systems of the experiments used to capture the outcomes of
¹⁶² the collisions will require upgrades to handle higher collision rates and background radiation
¹⁶³ rates than they were designed for.

¹⁶⁴ During the 2019-2022 Long Shutdown of the LHC, the most complex upgrade of the ATLAS
¹⁶⁵ experiment is the replacement of the small wheels of the muon spectrometer with the so-
¹⁶⁶ called New Small Wheels (NSWs) [5]. The NSW upgrade addresses both the expected

decrease in hit efficiency of the precision tracking detectors and the high fake trigger rate of the muon spectrometer. Two different detector technologies will be installed, stacked on the NSW frame: micromegas (MMs) and small-strip thin gap chambers (sTGCs). MMs are optimized for precision tracking while sTGCs are optimized for rapid triggering, although each will provide complete coverage and redundancy over the area of the NSW. Canada was responsible for providing 1/4 of the required sTGCs.

To reduce the fake trigger rate, the NSW will provide better track angular resolution to the ATLAS trigger system to reject tracks that do not originate from the collision [5]. sTGCs provide 100 μm position resolution per detector plane [6], and are stacked in four (called an sTGC quadruplet) to provide 1 mrad angular resolution on tracks [5, 7]. sTGCs are gas ionization chambers where a thin volume of gas is held between two cathode boards. One board is segmented into strip electrodes of 3.2 mm pitch. The position of the particle track in the precision coordinate can be reconstructed from the strip signals [5] to within the required position resolution [6].

Precise position resolution is naught without accurate positioning of readout electrodes in ATLAS. The ATLAS alignment system is able to position the surface of three sTGC or MM quadruplets traversable by a muon track with respect to one another within 40 μm . The internal geometry of the detectors must be controlled or corrected for to within the chambers' position resolution [5]. Corrections to the position of strip electrodes in sTGC quadruplets are in their final stages. The corrections are done with characterization data collected throughout the construction process. At the cathode board level, strip electrode positions are digitized with a coordinate measuring machine (CMM) [8]
I'm citing Carlson but should I be citing a paper that deals with the global context? E.g. something at the collaboration level. At the quadruplet level, sTGC quadruplets are characterized with cosmic rays over the whole area and with an x-ray gun at positions that will be tracked by the alignment system. Cosmic muon data (cosmics data) can be used to measure relative strip position offsets in a local area with respect to the strip patterns on other layers, which characterizes the strips' alignment but does not allow the strips to be positioned in the absolute ATLAS alignment system. The x-ray method [9] is able to measure offsets of the strip pattern near the x-ray gun in a coordinate system accessible to the alignment system; however, it is limited to a handful of positions on the surface of the quadruplet and should be validated by an independent method. In this work, cosmics data is used to measure relative strip offsets, the x-ray method is validated with cosmics data, and how this work fits into the overall alignment scheme is presented.

Chapters 2 and 3 give more background on particle physics, the LHC, ATLAS, the NSWs, and sTGCs. In chapter 4, the cosmic ray testing procedure and how the position of the strips can be probed with cosmics data is presented. Chapter 5 introduces the x-ray method, and

204 in chapter 6, the x-ray offsets are validated with cosmic muon data. The thesis concludes
205 with a summary and outlook in chapter 7.

²⁰⁶ Chapter 2

²⁰⁷ High energy particle physics at the ²⁰⁸ LHC and the ATLAS experiment

²⁰⁹ The LHC, ATLAS, and the upgrades they are undergoing are all motivated by the study
²¹⁰ of the SM and the open questions the SM does not address. Particle physics aims to study
²¹¹ the indivisible constituents of matter. Understanding the fundamental building blocks and
²¹² how they interact informs our understanding of the evolution of the Universe from the Big
²¹³ Bang to the forms of matter we recognize today. This chapter provides context for the NSW
²¹⁴ upgrade. The study of particle physics using accelerators is introduced, before moving on
²¹⁵ to the LHC, HL-LHC and the ATLAS experiment. The connection to physics questions of
²¹⁶ interest will be highlighted at each stage.

²¹⁷ The information on particle physics and the SM presented here is rather general; the reader
²¹⁸ is referred to [10, 11, 12] for more information.

²¹⁹ 2.1 The Standard Model

²²⁰ The SM describes all the fundamental particles and their interactions. It is a collection of
²²¹ quantum field theories able to explain the existence of all the particles discovered in the past
²²² century and predict how they interact to incredible precision. In fact, when it was being
²²³ developed in the 1960s-1970s, it began motivating the search for yet undiscovered particles,
²²⁴ like the tau neutrino with DONUT in 2002 [13].

²²⁵ The SM represented in figure 2.1, consists of six quarks, six leptons, and five force-particles.
²²⁶ Note that each particle also has an anti-particle, which are not represented. The force-
²²⁷ carrying bosons are exchanged between interacting (coupled) particles to produce what is

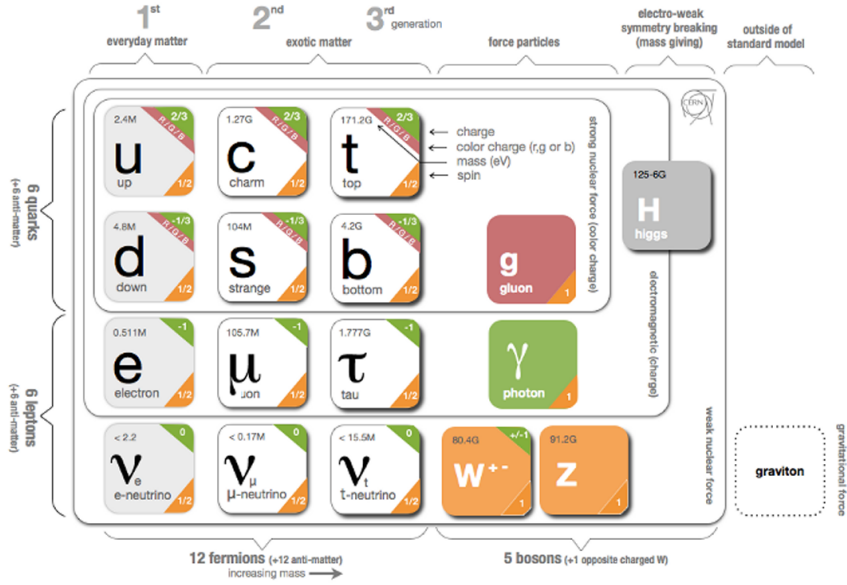


Figure 2.1: Representation of the SM of particle physics. There are three main types of particles: quarks, leptons and force-particles. The version highlights which groups of particles each force-particle interacts with. The force-particle in each black enclosure interacts with all quarks/leptons within the enclosure [14].

perceived as: the strong force mediated by gluons; the electromagnetic force mediated by photons; and the weak force mediated by the charged W-bosons and neutral Z-boson. The SM actually presents a theory of the electromagnetic and weak force as one force stemming from the same phenomenon: the unified electroweak force. The Higgs boson field interacts with the particles mediating the unified electroweak force to distinguish the weak and electromagnetic forces from each other and give all particles (except neutrinos) a mass. This is called electroweak symmetry breaking.

Quarks are fermions that are sensitive to all forces; notably they are the only particles sensitive to the strong force. Protons and neutrons are made up of quarks and gluons, and the strong force is responsible for their existence and mutual attraction into nuclei [15]. Leptons are particles not sensitive to the strong force. Charged leptons include the electron, which once part of atoms is responsible for chemistry. Neutrinos are neutral, almost massless particles that only interact through the weak force.

Common matter is made up of the lightest constituents of the SM: up and down quarks, electrons and photons. The other particles are or were generated in high-energy environments and decay eventually to the lightest constituents. Such high energy environments include the Big Bang [16], astrophysical sources, and accelerators. The presence of the particles of the SM at the beginning of the Universe means that their interactions and decays are fundamental for the study of the origin of the Universe [16]. Many high energy astrophysical sources, like supernovae, generate particles that rain down on Earth as cosmic rays [17]. Accelerators were built to create controlled, high energy and high rate environments where the production and decay of fundamental particles can be manufactured, detected and studied.

2.2 Beyond the Standard Model

The SM provides no explanation for several open questions in particle physics.

First, gravity is not included in the SM. One might expect a force-particle to exist that mediates the gravitational force, but the strength of gravity is so weak that the “graviton” will elude detection for a long time. Moreover, there is no theory of gravity that does not require dark energy or dark matter [12]. The universe is expanding at a rate irreconcilable with the known energy density of the Universe, and the nature of this “dark energy” is unknown [16]. Similarly, dark matter is the name given to mass in the universe whose gravity is measurable, but for which there is no SM explanation [18].

Second, neutrinos in the SM are massless; they do not interact with the Higgs field. However, in 2013 neutrino oscillations were confirmed, which can only occur if neutrinos do have mass [19].

262 Third, the unification of the electromagnetic and weak force begs the question of if there is
263 a Grand Unified Theory (GUT) that includes the strong force and encompasses the SM in a
264 more complete theory [20].

265 Theories beyond the standard model (BSM) aim to answer these questions. Often, BSM
266 theories predict new particles. For example, super-symmetry (SUSY) predicts that each
267 SM particle has a heavier super-symmetric partner. SUSY would explain the origin of dark
268 matter with weakly interacting massive particles, would solve the so-called "naturalness"
269 problem in the SM at energies above the tera-electronvolt scale, and is often a part of
270 GUTs [21]. Ideally, a BSM theory predicts a measurable signature that can be searched for
271 at accelerators or elsewhere.

272 **2.3 Studying high energy particle physics with accelerators** 273

274 Accelerators of increasingly high energy have a long history of enabling the discovery of new
275 particles. Only calling on one example, one of the main goals when the LHC, the ATLAS
276 experiment and the CMS experiment were proposed was to detect the long-predicted Higgs
277 boson particle – a triumph accomplished in 2012 [22, 23]. Being the last particle of the SM
278 to be discovered, the discovery marked the completion of the SM as it is known today.

279 Since then, measurements of the cross section of particle physics processes have been enabled
280 by the LHC. A summary of the cross sections measurements done at the ATLAS experiment
281 is shown in figure 2.2. Given the precision to which the SM predicts cross sections and the
282 precision to which many can be measured, any discrepancy between theory and experiment
283 could be an indication of new physics. The questions the SM does not address require new
284 physics; searching for it at accelerators is a natural choice.

285 Accelerators and detectors can also be used to search for signatures of rare processes predicted
286 by the SM and BSM theories. The controlled, high rate environment enables the search for
287 signatures that would be impossible to discern in other environments. If the signature is not
288 found, exclusion limits can be set [25].

289 Through measurements and searches, accelerators play a key role in making precision mea-
290 surements, searching for rare processes predicted by the SM, and testing BSM theories.

291 *Is there a good citation for the defintion of search vs measurement?*

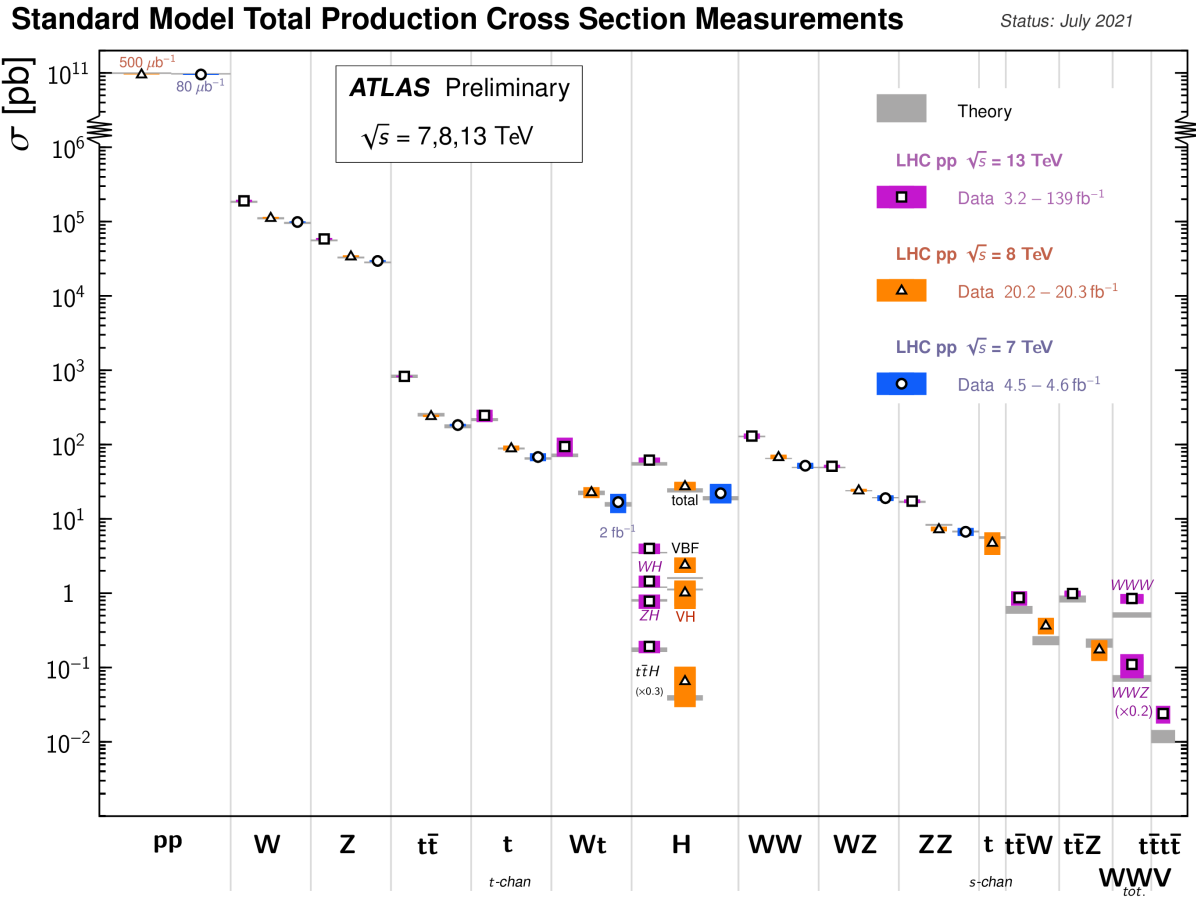


Figure 2.2: Cross sections of select SM physics interactions measured using the ATLAS experiment at the LHC. The comparison with theoretical predictions is also shown [24].

292 2.4 The Large Hadron Collider

293 The LHC is an accelerator 27 km in circumference and located \sim 100 m underground at
294 CERN near Geneva, Switzerland [1]. It has two beam pipes that counter-circulate bunches
295 of protons¹ before colliding the bunches in the center of one of four major experiments, such
296 as the ATLAS experiment (discussed in section 2.7). In the previous run of the LHC (run-2),
297 protons were collided with a center of mass energy of 13 TeV. It is not actually the protons
298 that interact, but the constituent quarks and gluons (partons) that each carry some fraction
299 of the energy and momentum of the collisions.

300 2.5 Luminosity

301 The number of proton-proton interactions generated by the LHC directly affects the statis-
302 tics available to make measurements of cross sections, SM parameters, etc. Predicting the
303 number of proton-proton interactions requires defining a metric called luminosity [12]. It is
304 the number of particles an accelerator can send through a given area per unit time. It is
305 calculated from the measurable quantities in equation 2.1:

$$\mathcal{L} = \frac{f N_1 N_2}{4\pi\sigma_x\sigma_y} \quad (2.1)$$

306 f is the frequency of the bunch crossings (25 ns), N_1 and N_2 are the number of protons in
307 each bunch ($\sim 10^{11}$ protons / bunch), and σ_x and σ_y are the RMS of the spatial distributions
308 of the bunch. Therefore, luminosity is a property of accelerator beams, which are set by the
309 capabilities of the accelerator. The design luminosity of the LHC was 10^{34} cm $^{-2}$ s $^{-1}$. The
310 units of luminosity are an inverse area; multiplying the luminosity by the cross section of a
311 given process gives the expected rate for that process.

312 Integrating the *instantaneous* luminosity (equation 2.1) over a period of data collection gives
313 the integrated luminosity,

$$L = \int \mathcal{L}(t) dt \quad (2.2)$$

314 which is related to the total number of interactions. In this way, the luminosity is the link
315 between the accelerator and the statistical power of measurements to be made with the data

316¹the LHC also accelerates lead ions, but ATLAS is best at recording proton-proton collisions. The ALICE
317 experiment [26] was designed for lead-lead interactions.

316 collected. So far, the LHC provided an integrated luminosity of 28.26 fb^{-1} in run-1 [27] and
317 156 fb^{-1} in run-2 [28].

318 2.6 The High-luminosity LHC

319 The HL-LHC upgrade [2] was accepted because without increasing the luminosity of the LHC
320 tenfold, running the accelerator will not provide significant statistical gain on measurements.
321 Also, some systems will need repair and replacement to operate past ~ 2020 . The LHC will
322 be the most energetic accelerator in the world for years to come and is the only accelerator
323 capable of directly producing the Higgs boson (and top quarks), so the European Strategy for
324 Particle Physics made it a priority “to fully exploit the physics potential of the LHC” with
325 “a major luminosity upgrade” [29]. The goal is for the HL-LHC to provide an integrated
326 luminosity of 3000 fb^{-1} in the 12 years following the upgrade. The luminosity actually
327 achieved will depend on a combination of technological advances and upgrades in progress
328 that affect the factors contributing to luminosity defined in equation 2.1 [2].

329 The most anticipated measurement at the HL-LHC is of the triple-Higgs coupling. Measuring
330 the coupling allows the shape of the Higgs potential responsible for electroweak symmetry
331 breaking to be measured. Any discrepancy with the SM prediction will show that there
332 must be other sources of electroweak symmetry breaking, and hence currently unpredicted
333 particles. The LHC is the only accelerator where the Higgs can be produced directly and
334 the HL-LHC upgrade is required to have sufficient di-Higgs production to make a meaning-
335 ful measurement [4, 31]. Accordingly, detector sensitivity to various Higgs decays will be
336 important at the HL-LHC.

337 2.7 The ATLAS experiment

338 The ATLAS experiment [3] was designed to support all the physics goals of the LHC. It is
339 44 m long and 25 m in diameter, and weighs 7000 tones. It is an array of particle detector
340 subsystems arranged concentrically around the beam pipe and centered around one of the
341 LHC’s interaction points (a place where the beams collide), as shown in figure 2.4. ATLAS is
342 cylindrical because it aims to provide 4π coverage around the interaction point. It is helpful
343 to separate the subsystems of ATLAS into the so-called “barrel” and “endcap” / “forward”
344 regions, referring to the cylindrical geometry.

345 For analysis, ATLAS is typically described in spherical coordinates. The azimuthal angle
346 ϕ is measured around the beampipe and the polar angle θ is measured from the beam



Figure 2.3: LHC/HL-LHC plan [30]. The integrated luminosities collected and projected for each run of the LHC are shown in blue boxes below the timeline and the center of mass energy of the collisions is shown in red above the timeline. The top blue arrow labels the run number. “LS” stands for “long shutdown” and indicates periods where the accelerator is not operating. During the shutdowns, upgrades to the LHC and the experiments are being installed. This timeline was last updated in January, 2021, and reflects changes in the schedule due to the ongoing pandemic.

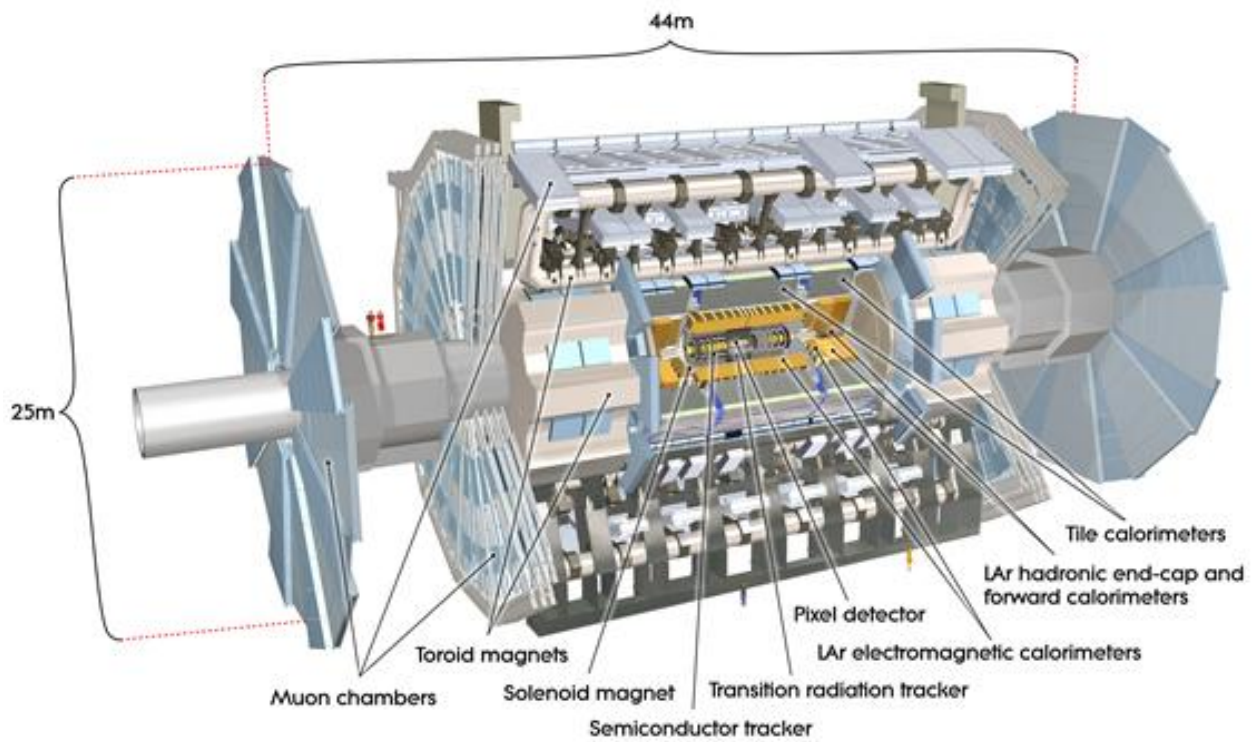


Figure 2.4: Diagram of the ATLAS experiment, with the various detector subsystems labelled [3].

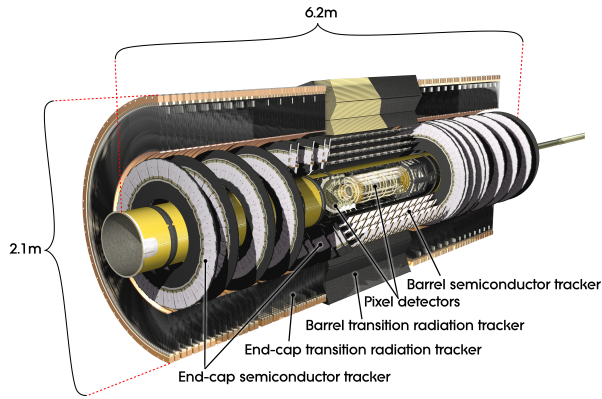


Figure 2.5: Diagram of the ATLAS experiment’s inner detector, with the different segments and the technology used labelled [3].

347 pipe. A more useful coordinate than θ is the pseudo-rapidity, $\eta = -\ln \tan(\theta/2)$, because
 348 it approaches the rapidity of a particle when its momentum is much greater than its mass
 349 and differences in rapidity are approximately invariant to a Lorentz boost parallel to the
 350 beam. The range of η is 0 (perpendicular to the beam) to $\pm\infty$ (parallel to the beam, or the
 351 z-direction). Typically, η is the physically interesting coordinate because the ϕ coordinate
 352 follows the cylindrical symmetry of the beam.

353 ATLAS provides identification and kinematic measurements for each particle created after
 354 the initial collision. Predictions made using SM and BSM theories can then be compared
 355 to the data. Each subsystem of ATLAS collects certain information and a complete
 356 description of each recorded collision can be assembled offline. An overview of the main
 357 ATLAS subsystems is given below.

358 **The inner detector**

359 The inner detector [32, 33] (figure 2.5) is for precision tracking, vertex measurements and
 360 electron identification. A 2 T solenoid with field parallel to the beam bends the track of
 361 outgoing particles. The innermost part is made of high-resolution semiconductor pixel and
 362 strip detectors while the outermost part are straw-tubes that generate and detect transition
 363 radiation

364 **Calorimetry system**

365 Electromagnetic and hadronic sampling calorimeter units are used to record the energy
 366 of electrons, photons and jets. A combination of liquid-argon (LAr) electromagnetic and

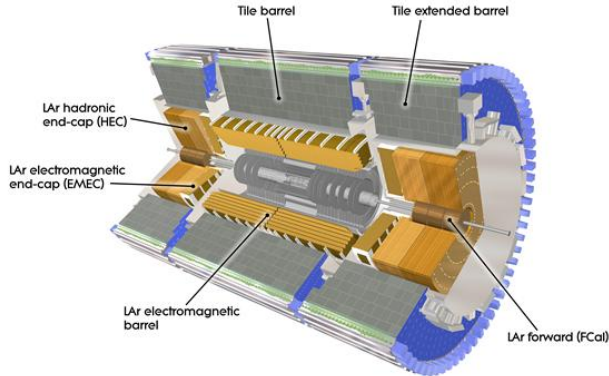


Figure 2.6: Diagram of the ATLAS calorimeter system, with the different segments and the technology used labelled [3].

367 hadronic calorimeters [34] and tile-scintillator hadronic calorimeters [35] cover the rapidity
 368 range $|\eta| < 4.9$, as shown in figure 2.6.

369 The calorimeters cause incoming charged particles to shower and deposit their energy in
 370 the sensitive volume. Only muons and neutrinos are known to pass the calorimeters to the
 371 muon spectrometer. Particles other than those mentioned would have decayed in the inner
 372 detector before reaching the calorimeter.

373 Trigger system

374 It would be impossible to record all the data from bunch crossings every 25 ns, corresponding
 375 to a rate of ~ 40 MHz. ATLAS has a multi-level trigger system to select events of interest
 376 for permanent storage. The Level-1 (L1) hardware trigger [36] uses partial-granularity infor-
 377 mation from the muon spectrometer and calorimeter to trigger on high p_T muons, electrons,
 378 jets, high missing transverse energy, and τ decaying to hadrons. The maximum L1 trigger
 379 rate ATLAS can accommodate is 100 kHz with a latency of 2.5 μ s. After run-3 an upgrade
 380 of the trigger system will allow for a higher rate and more latency, but for now these are the
 381 working limits [37].

382 The L1 trigger is used to define regions of interest that are fed into the software high level
 383 trigger (HLT), in which the full granularity of the muon spectrometer and calorimeter are
 384 used with information from the inner detector to reduce the trigger rate to 1 kHz. Events
 385 that pass the L1 and HLT trigger are recorded for use in offline analysis [38].

386 The ATLAS trigger system is described in the references above but the trigger rates quoted
 387 here are after the upgrades implemented for run-2, described in [39].

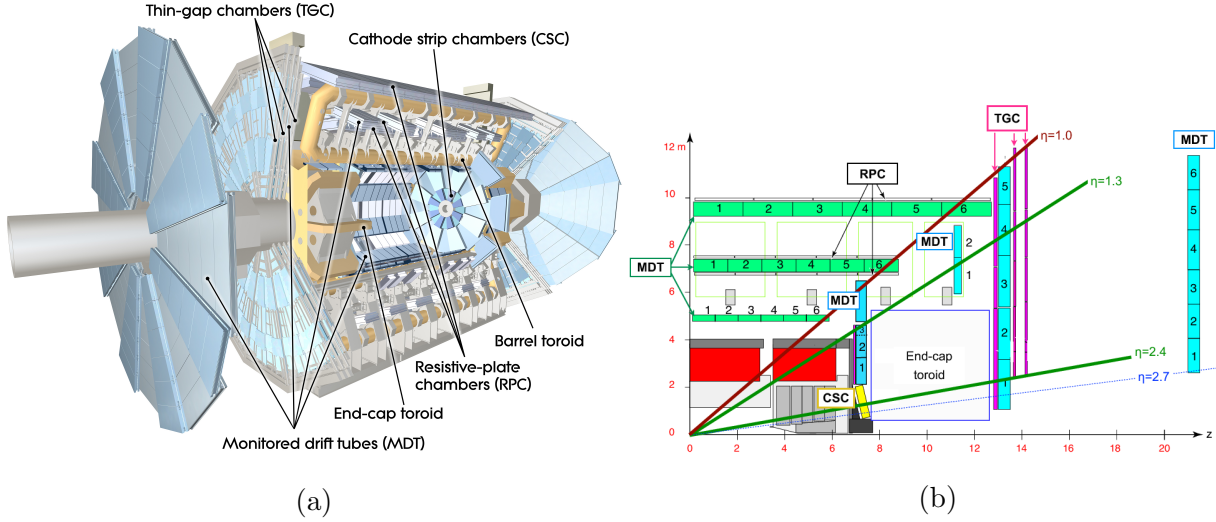


Figure 2.7: (a) The ATLAS muon spectrometer [3]. (b) A quarter-cut of ATLAS, with the interaction point in the bottom left corner. The small wheel is just left of the end cap toroid, the big wheel is to its right, and the outer wheel is the rightmost structure [41].

388 Muon spectrometer

389 The muon spectrometer has multiple layers, each of which records the position of a passing
 390 muon. Magnetic deflection by superconducting air-core toroid magnets bend the muon
 391 tracks. The position information recorded in each layer and the magnetic field are used to
 392 reconstruct each muon's momentum. In the barrel of ATLAS, eight coils bent into “race-
 393 tracks” arranged around the beampipe provide the magentic field. In the forward region,
 394 two end-cap toroids each with eight smaller racetrack-shaped coils arranged symmetrically
 395 around the beampipe are inserted in the ends of the barrel toroid [40]. Figure 2.7 shows the
 396 toroid magnets and the different parts of the ATLAS muon spectrometer [3].

397 The muon spectrometer [42] is separated into detectors used for precision offline tracking
 398 and for triggering. Three layers of monitored drift tubes (MDTs) or cathode strip chambers
 399 (CSCs) are used for tracking. The position of the muon track in each of the three layers allows
 400 reconstruction of the track and hence momentum. For the design momentum resolution of
 401 $\Delta p_T/p_T < 1 \times 10^{-4}$ p / GeV for $p_T < 300$ GeV and a few percent for lower p_T muons,
 402 the MDTs and CSCs required position resolution of 50 μm each. Accordingly, an optical
 403 alignment system was designed to monitor and correct for chamber positions [42, 43].

404 Resistive plate chambers (RPCs) are used for triggering in the barrel and thin-gap chambers
 405 (TGCs) are used for triggering in the endcaps. The positions of each type of chamber are
 406 sketched in figure 2.7b. Often, the endcap muon spectrometer is separated into three wheels –

407 the small wheel, big wheel, and outer wheel – ordered by proximity to the interaction point.
408 In run-1, low (high) p_T muons were triggered on at L1 if two (three) of the RPCs or TGCs
409 layers around the big wheel fired in coincidence, for the barrel and endcaps respectively [36].
410 After run-1 it was discovered that up to 90% of the triggers in the endcap were fake, caused
411 by background particles generated in the material between the small wheel and the big
412 wheel [5]. To reduce the fake rate in run-2, the TGCs on the inside of the small wheel also
413 had to register a hit. The added condition reduced the trigger rate by 50% in the range $1.3 < |\eta| < 1.9$ [39]. The effectiveness of the solution was limited since the $|\eta|$ -range of the small
415 wheel TGCs was limited to $1.0 < |\eta| < 1.9$ and the position resolution of the small wheel
416 TGCs is coarse [5].

417 **Chapter 3**

418 **The New Small Wheels**

419 **3.1 Motivation for the New Small Wheels (NSWs)**

420 The hit rate of all detector systems will increase with the HL-LHC not only because of the in-
421 crease in luminosity, but also because the background radiation rate increases proportionally
422 with luminosity. The combined rate presents problems for both the tracking and triggering
423 capabilities of the muon spectrometer [5].

424 In term of tracking, the efficiency of the MDTs decreases by 35% (mostly due to long dead-
425 times) already when exposed to the maximum hit rate at the current luminosity, 300 kHz.
426 At the threefold increase in luminosity predicted for run-3, most of the small wheel will be
427 subjected to a hit rate well above 300 kHz and it will begin missing hits. Losing hits in the
428 small wheel will reduce the high p_T muon momentum resolution. The decrease in resolution
429 will affect the ability to search for, for example, the decay of heavy bosons (W' , Z') or a
430 pseudo-scalar Higgs predicted by some SUSY models [4].

431 Already, the forward muon trigger system copes with a very high fake rate, even when
432 including TGC data from the small wheel in the trigger as in run-2. At the luminosity
433 expected in run-3, 60 kHz of the maximum 100 kHz of the L1 trigger would be taken by the
434 endcap muon spectrometer. A possible solution would be to raise the minimum p_T threshold
435 from 20 GeV to 40 GeV, but the ability to study several physics processes of interest depend
436 on low p_T muons, particularly the Higgs decay to two muons, the Higgs decay to two tau's
437 and SUSY particle decays to leptons [5].

438 The NSWs will solve both these problems. It will be covered with precision tracking cham-
439 bers suitable for the expected hit rates and triggering chambers capable of 1 mrad angular



Figure 3.1: A schematic of a quarter cross section of the ATLAS detector, with the collision/interaction point (IP) in the bottom left corner. Three possible tracks are labelled. Ideally, track A would be triggered on while track B and C discarded. With the small wheel, all three tracks would be recorded. With the NSW, only track A would be recorded [5].

resolution. The idea behind the triggering chambers is to match the small wheel track segment with the track segment from the big wheel to discard tracks not originating from the interaction point. Figure 3.1 illustrates this point: the run-1 trigger system would have triggered on all three tracks, while with the NSW the trigger system would only trigger on track A. Reducing the fake trigger rate means the NSWs will not miss as many muon hits and that the low p_T threshold will not have to be raised to cut particles not produced in the collision. The NSWs allow ATLAS to maintain the high p_T muon resolution and the low muon p_T threshold at the HL-LHC collision rate [5].

448 **3.2 Design of the NSWs**

449 The NSWs are covered with two detector technologies: micromegas and small-strip thin gap
450 chambers. MMs are the primary tracking detectors and sTGCs are the primary triggering
451 detectors, but for redundancy sake both are designed to do either. Both sets of detectors are
452 to have position resolution better than $\sim 100 \mu\text{m}$ per plane. Four chambers of each type are
453 glued together to create quadruplet modules. Quadruplets of different sizes are assembled
454 into wedges. Two sTGC wedges and two MM wedges are layered to create sectors (with
455 the sTGC wedges on the outside) [5]. Different stages of the construction process are shown
456 in figure 3.2. At the time of writing, both NSWs have been assembled. The first has been
457 lowered into the ATLAS cavern and is being commissioned. The second will be lowered
458 shortly.



(a) An sTGC quadruplet module. The left image highlights the trapezoidal shape. The right image shows the short edge corner. The four sTGC layers and each layer's gas inlet are visible. The gas outlets and high voltage cables are at the long edge in the back of the photo. The green printed circuit board along the sides are the adaptor boards where the front end electronics are attached.



(b) Left: An sTGC wedge. The white frame outlines the individual quadruplet modules. Right: A completed sector, with two sTGC wedges on the outside and two MM wedges on the inside.



(c) The New Small Wheel. All sectors except one large sector at the top are installed, revealing two of the smaller sectors that are normally hidden under the large sectors and support bars. The NSWs are 10 m in diameter.

Figure 3.2: Images breaking down some of the construction units of the NSWs.



Figure 3.3: Internal structure of an sTGC, zoomed into the area under a pad. High voltage is applied to wires suspended in the gas volume to create an electric field. A passing muon causes an ionization avalanche that is picked up by the wire, strip and pad electrodes [9].

459 3.3 Small-strip thin gap chambers

460 sTGCs are gas ionization chambers operated with a CO₂:n-pentane ratio of 55:45. Gold-
461 plated tungsten wires, 50 µm in diameter and with 1.8 mm pitch, are suspended between
462 two cathode planes made of FR-4, each 1.4 mm away (see figure 3.3). One cathode board is
463 segmented into pads of varying area (around 300 cm² each), and the other segmented into
464 strips of 3.2 mm pitch, perpendicular to the wires. High voltage is applied to the wires and
465 the cathode planes are grounded [5, 7]. When a muon passes through, the gas is ionized and
466 the electric field in the gas gap causes an ionization avalanche [44]. The motion of the ions
467 and electrons are picked up on the nearby wire, strip and pad electrodes [5]. The gas mixture
468 was chosen to absorb excess photons produced in the avalanche that delocalize the avalanche
469 signal [45]. The resistivity of the carbon coating and capacitance of the pre-preg sheet tune

470 the spread of the charge distribution [46] and the speed of the response [47] to optimize
471 the rate capability. The hatching of the strips and wires establishes a coordinate system
472 from which to extract the coordinate of the muon as it passes through the chamber. The
473 small pitch of the strips is what allows the quadruplets to deliver good angular resolution to
474 improve the fake trigger rate and meet the precision tracking requirements [5].

475 A 3-out-of-4 coincidence in pad electrodes from each layer of a quadruplet define a region of
476 interest where the strip and wire electrodes should be readout. The pad triggering scheme
477 greatly reduces the number of electrodes that require read-out so that a track segment of
478 the required angular resolution can be provided quickly enough to the hardware trigger [5].

479 Signal is readout from groups of successive wires, so the position resolution in the direction
480 perpendicular to the wires is 10 mm. The wires give the symmetric azimuthal coordinate in
481 ATLAS so the position resolution in this direction is sufficient. Good resolution on the η
482 coordinate, perpendicular to the strips, is important [5]. The average single chamber position
483 resolution in the strip coordinate was 45 μm for perpendicular muon tracks as measured in a
484 test beam [6] – well within design specifications. When four sTGCs are glued together into a
485 quadruplet the design angular resolution of 1 mrad in the strip coordinate is achievable [5, 7].

486 Therefore, sTGCs are able to meet the triggering and precision tracking goals they were
487 designed for. To ensure they can deliver once installed in ATLAS, knowing the position of
488 the strips to within their position resolution in the ATLAS coordinate system is necessary.
489 The NSW alignment system, detailed in section 3.5, monitors the position of alignment
490 platforms installed on the surface of the wedges. The alignment platforms are installed with
491 respect to an external reference on the sTGCs: two brass inserts on each strip layer on one
492 of the angled sides of each quadruplet (shown in figure 3.4). So the challenge of positioning
493 the strips in ATLAS was separated into two steps: first, position the strips with respect to
494 the brass inserts; second use the alignment system to position the alignment platforms. The
495 next section provides some pertinent details on the sTGC construction process, with steps
496 that affect the position of the strips with respect to the brass inserts highlighted.

497 3.4 sTGC Quadruplet Construction

498 Five countries were responsible for producing the sTGC modules of varying geometries for
499 the NSW: Canada, Chile, China, Israel and Russia. Canada was responsible for 1/4 of the
500 required sTGCs, of three different quadruplet geometries. The steps of the construction
501 process in each country were similar [5]. The process followed in Canada is detailed.
502 TRIUMF in Vancouver, British Columbia was responsible for preparing the cathode boards.
503 The boards were made and the electrodes etched on at a commercial laboratory, Triangle



(a) Brass insert near long edge.

(b) Brass insert near short edge.

Figure 3.4: The brass inserts sticking out from the gas volumes of an sTGC quadruplet. These inserts were pressed against alignment pins when the individual sTGCs were being glued together.

504 Labs, in Carson City, Nevada. Once completed they were sent to TRIUMF to be sprayed with
505 graphite and otherwise prepared [8]. The boards are commercial multilayer printed circuit
506 boards, but the strip boards required precision machining to etch the strip pattern [5].
507 Triangle Labs also machined the two brass inserts into each strip board. A coordinate
508 measuring machine (CMM) was used to digitize a set of reference strips. Four quality
509 parameters describing non-conformities in the strip pattern of each board with respect to
510 the brass inserts were derived from the data and the results are available on a QA/QC
511 database. The parameters and the CMM data collection is described in full in [8]. Due to
512 time constraints, tolerances on the non-conformities in the etched strip pattern with respect
513 to the brass inserts were loosened, with the condition that the strip positions in ATLAS
514 would have to be corrected for [8].

515 The prepared boards were sent to Carleton University in Ottawa, Ontario for construction
516 into sTGCs and quadruplets. First, the wires were wound around the pad cathode boards
517 using a rotating table and the wires were soldered into place. A wound pad cathode board
518 was held by vacuum on a granite table, flat to within 20 μm , and a strip cathode board glued
519 on top to create an sTGC. Holding one sTGC flat with the vacuum, another was glued on
520 top to create a doublet, then two doublets were glued together to create a quadruplet. When
521 gluing sTGCs together, the brass inserts were pushed against alignment pins with the goal of
522 keeping the strip layers aligned within tolerance. However, non-conformities in the shape of
523 the brass inserts, non-conformities in the position of the alignment pins and shifts between
524 sTGCs while the glue cured resulted in misalignments between the brass inserts and strip
525 layers. Precise alignment of the pad boards or wires with respect to the strip boards did not
526 have to be so tightly controlled because pads do not measure the precision coordinate.

527 The Carleton team finished the quadruplets by installing adaptor boards on the angled sides
528 of each layer that allow front end electronics to be attached. Completed quadruplets were
529 sent to McGill University where they were characterized with cosmic rays. The details of
530 cosmic ray testing are described in chapter 4. Tested quadruplets were sent to CERN where
531 they were assembled into wedges and alignment platforms installed. The alignment platforms
532 were installed using a jig positioned with respect to the brass inserts. Completed wedges
533 were assembled into sectors then installed on the NSWs.

534 The quadruplet construction process had two steps where strip positions could be shifted off
535 of nominal. At board-level, there could be non-conformities in the etched strip pattern with
536 respect to the brass inserts, described by the four quality parameters [8]. At the quadruplet
537 level, misalignments between the brass inserts and strips on different layers were introduced
538 during the gluing. The result was that the brass inserts were not a reliable reference point
539 and that the strips can be offset from their design position by up to hundreds of micrometers.
540 Offsets in strip positions from nominal in Canadian quadruplets were shown to be random [8],

541 so no one correction would suffice. The offsets must be measured and corrected for in the
542 ATLAS offline software that does the precision tracking. Understanding the work ongoing
543 to make measurements of offsets and correct for them requires understanding the strategy
544 of the NSW alignment system.

545 3.5 NSW alignment

546 The idea of the NSW alignment system is presented in [5], but the details have only been
547 presented internally so far. After the wedges are constructed, alignment platforms are in-
548 stalled on every sTGC quadruplet and optical fibres routed to them, as shown in figure 3.5.
549 Light from the optical fibres will be monitored in real time by cameras (BCAMs) mounted on
550 the alignment bars of the NSWs. The system will thus record the positions of the alignment
551 platforms in the ATLAS coordinate system, accessible at any point during operation.

552 The original alignment scheme was to use the brass inserts as a reference between the align-
553 ment platforms and the individual strips, as shown in the solid arrows in figure 3.6 – this
554 will no longer work. The position of the alignment platforms will be known thanks to the
555 alignment system, so a different method to get the position of the strips with respect to
556 the alignment platforms is currently in its final stages. It uses the yet-unmentioned x-ray
557 dataset to calculate offsets of the strip pattern of an sTGC layer in a local area (local offset)
558 with respect to the nominal geometry by analyzing the beam profile left by an x-ray gun
559 attached to different positions on the alignment platforms. Effectively, the reference to the
560 brass inserts is skipped, represented as the dashed line in figure 3.6. The alignment plat-
561 forms provide the link to the nominal geometry because their position with respect to the
562 strips can be calculated from the nominal geometric parameters assuming that the strips
563 are perfectly etched and aligned. Cosmic muon track positions cannot be compared to the
564 nominal geometry because the alignment platforms are not installed when cosmics data is
565 collected, so there is no external reference to provide a link to the nominal geometry.

566 The x-ray method does not have the sensitivity to measure the offset of each strip from
567 nominal, but instead the offset of the strip pattern in a local area around the position of
568 the gun can be measured. *Local offsets* are used to build an alignment model for each strip
569 layer. Formally defined, an alignment model is a set of parameters used to estimate the true
570 position of a strip given its nominal position. The alignment model currently being worked
571 on takes x-ray and CMM data as input to calculate an offset and rotation of each strip
572 layer with respect to nominal [9]. The alignment parameters could be described as “global”,
573 meaning over the whole layer instead of local. Without the x-ray dataset, there would be no
574 input to the alignment model that takes into account inter-layer misalignments introduced

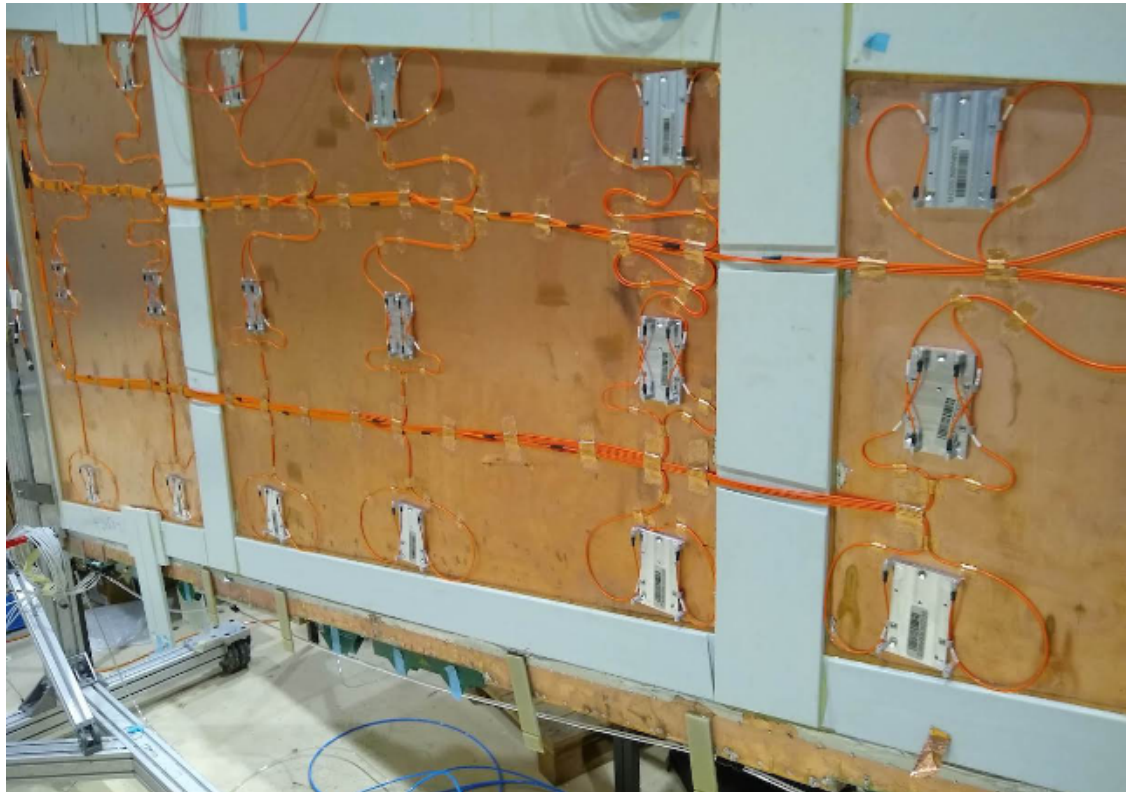


Figure 3.5: An sTGC wedge with alignment platforms (silver) installed on the quadruplet. Optical fibres (orange) are routed to the alignment platforms. Cameras on the frames of the NSWs will record light from the optical fibres to position the alignment platforms in the ATLAS coordinate system.

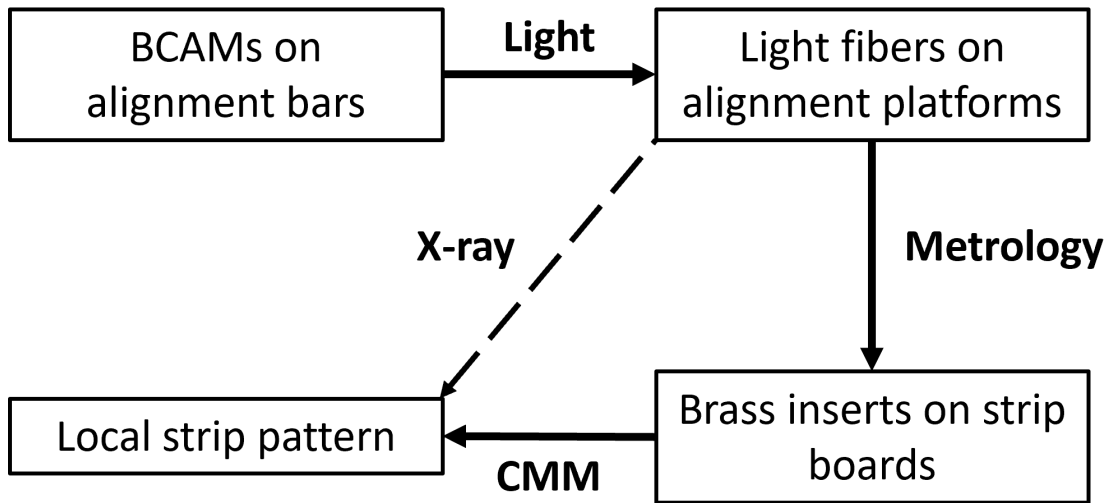


Figure 3.6: How the different elements of the sTGC alignment system relate to one another. The solid arrows denote the planned alignment scheme. The dashed arrow shows the modification being finalized now. This figure was originally designed by Dr. Benoit Lefebvre.

⁵⁷⁵ in construction.

⁵⁷⁶ Given that the x-ray local offsets can only be measured at positions where the gun can be
⁵⁷⁷ attached and that they are an important part of the alignment scheme, the x-ray method
⁵⁷⁸ needs to be validated. The goal of this thesis is to validate the x-ray local offsets while
⁵⁷⁹ exploring how cosmics data complements and adds to the understanding of strip positions
⁵⁸⁰ and overall alignment.

581 **Chapter 4**

582 **Using cosmic muons to measure
583 relative strip position offsets**

584 At McGill, among other quality and functionality tests, each Canadian-made quadruplet was
585 characterized with cosmic muons. In this chapter, the experimental setup and how the data
586 was analyzed to provide relative strip position offsets is presented. The analysis method
587 was motivated by the how it could be compared to data collected with the x-ray method
588 (chapter 5) but also stands alone as a characterization of the alignment between strips of
589 different layers. First, a brief introduction to cosmic rays.

590 **4.1 Cosmic rays**

591 The Earth is being bombarded by particles from the sun, galactic sources and extra galactic
592 sources – collectively called cosmic rays [17, 12]. Cosmic rays are mostly protons, but also
593 heavier ions, gamma rays and the term sometimes includes neutrinos. The primary (initial)
594 cosmic ray interacts with the atmosphere causes electromagnetic and hadronic showers of
595 particles. Hadronic showers result from the primary cosmic ray interacting strongly with the
596 target of the atmosphere and the most abundant products are pions. Charge pions mostly
597 decay to muons (there is a lesser contribution to the muon flux from kaons as well) [48].
598 Thanks to time dilation extending the muon’s lifetime as measured on Earth, a flux of
599 approximately 1 muon/cm²/ min reaches the ground [12]. Measuring the muon flux and
600 energy spectrum reveals information about primary cosmic rays [48] which is interesting to
601 high energy physicists and astrophysicists. The muon flux is also terribly convenient for
602 testing muon detectors.

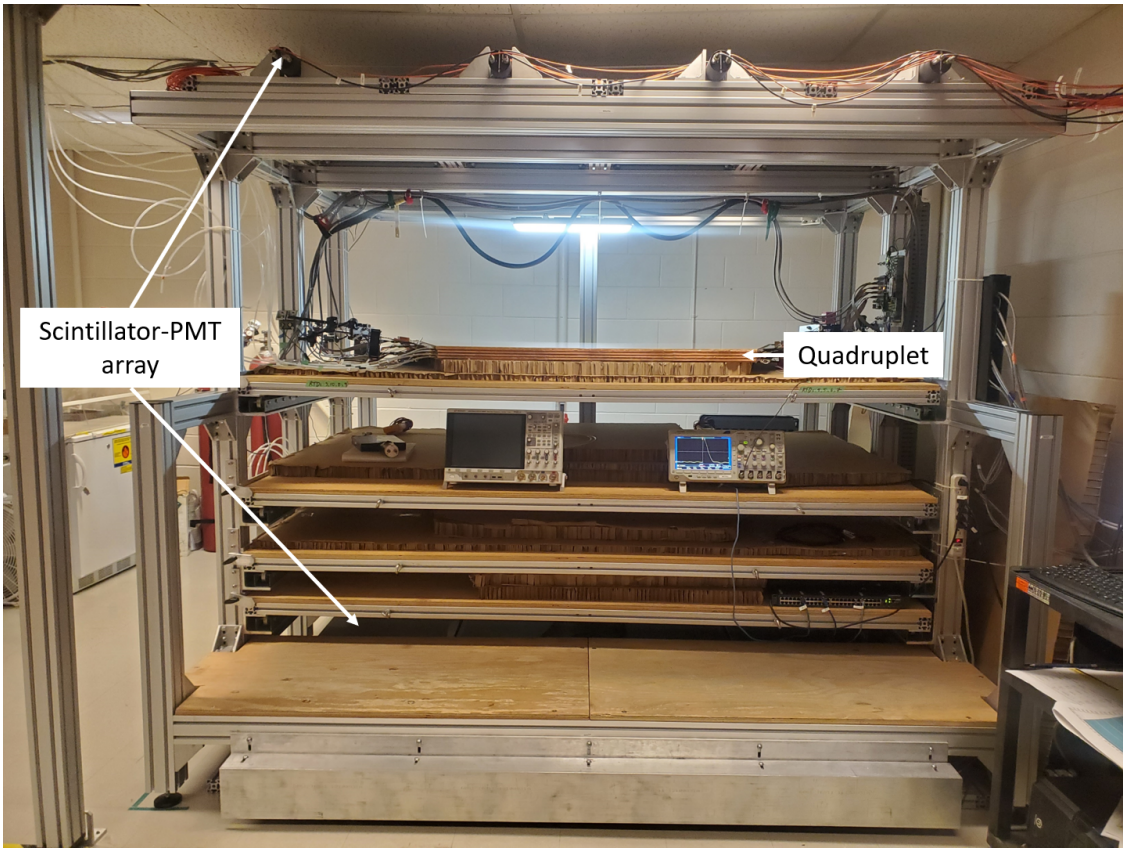


Figure 4.1: Cosmic muon hodoscope at McGill University with sTGC quadruplet in the test bench.

603 4.2 Experimental setup

604 Cosmic muon characterization was done with a hodoscope, a complete description of which
 605 can be found in [49]. The quadruplet was placed in the center of the test bench. Above
 606 and below it was a layer of scintillator-PMT arrays, labeled in figure 4.1. When a cosmic
 607 muon passed within the acceptance of the hodoscope, at least one scintillator from the top
 608 array and at least one from the bottom array fired in coincidence. The coincident signal was
 609 used to trigger the readout of the quadruplet's electrodes using NIM modules. The trigger
 610 was passed to the front-end electronics attached to the adaptor boards of each layer of the
 611 quadruplet.

612 Operating the chambers also required gas and high voltage. A pentane-CO₂ mixture was
 613 mixed and delivered to each sTGC with a gas system designed and made at McGill University.

614 The gas system was controlled by a slow control program, also made in-laboratory [50].
615 Although gas mixture is flammable, it allows the chambers to operate in high amplification
616 mode without production of excess photons saturating the signal across many strips because
617 pentane absorbs a wide energy of photons [45]. To prepare the quadruplets for operation,
618 CO_2 was flushed through them overnight to remove impurities. Then, five gas volumes of
619 the pentane- CO_2 mixture was flushed through (approximately 3 hours). High voltage was
620 provided by CAEN boards.

621 4.3 Data acquisition

622 Each sTGC electrode was connected to a channel on a prototype ASIC¹ on the front-end
623 electronics, attached to the adaptor boards on each layer of a quadruplet. The ASIC ampli-
624 fied the signal and was set to measure and record the signal peak amplitude from electrodes.
625 For each trigger, the signal peak amplitude of all channels above threshold was recorded
626 as an event and stored in a binary file. Channel thresholds were estimated [52] and ad-
627 justed manually in the configuration/readout software before the start of data acquisition.
628 There was an exception to the threshold rule: the signals on strips adjacent to a strip above
629 threshold were also readout using the so-called “neighbour triggering” function of the ASIC.
630 The quadruplets were held at 3.1 kV for approximately two hours to collect data from 1
631 million muon triggers.

632 4.4 Data preparation

633 4.4.1 Cuts on electrode hits

634 Corrupted data is removed while the raw data is being recorded in a binary file. The binary
635 file is decoded into a usable ROOT [53] tree offline.
636 A hit is defined as a signal recorded from a channel that was above threshold or (in the
637 case of strips) neighbour triggered. In addition to hits from muons, the quadruplets record
638 noise from the electronics and δ -rays (electrons liberated with sufficient energy to cause more
639 ionization before acceleration). Therefore, cuts are applied to reduce the number of noise
640 hits. The edge strips are very noisy, so all strip hits on layers with strip hits on either
641 edge channel are cut. A default pedestal value is subtracted from the recorded signal peak

¹the VMM3 [51], designed for the MMs and sTGCs of the NSW

642 amplitude of each electrode for a more realistic estimate of the signal amplitude. Also, events
643 that only have hits on pad electrodes (no strips or wires) were cut because the large area of
644 the pads made them susceptible to noise.

645 **4.4.2 Clustering and tracking**

646 Many of the high-level characterization metrics require rebuilding muon tracks. For events
647 passing quality cuts, the x - and y -coordinates of the ionization avalanche on each layer are
648 extracted from the signal on the wires and strips respectively for each event, as is sketched in
649 figure 4.2. In this work, x is the coordinate perpendicular to the wires and y is the coordinate
650 perpendicular to the strips.

651 The x -coordinate is taken as the center of the wire group with the maximum peak signal
652 amplitude, since the wire groups' pitch (36 mm) is larger than the typical charge spreading.
653 Assuming that the true x -position of the hit is sampled from a uniform distribution over the
654 width of the wire group, the uncertainty in the x -position was given by $\frac{36}{\sqrt{12}}$ mm = 10 mm [54].

655 The y -coordinate is taken as the Gaussian mean of the peak signal amplitude distribution
656 across groups of contiguous strips. The process of grouping contiguous strip hits on a layer is
657 called clustering, and the resulting group is called a cluster. Figure 4.2 sketches the clustering
658 process and a sample cluster is shown in figure 4.3. The data acquisition system recorded
659 the electrode ID of the strip hit and in the clustering process the position of the center
660 of the strip electrode is calculated based on the nominal quadruplet geometry. Typically,
661 clusters are built of 3-5 strips. The thickness of the graphite coating over the cathode boards
662 determined how many strips picked up the ionization image charge. Larger clusters were
663 more likely caused by δ -rays since they spread the cloud of ionization.

664 Events are cut from the analysis if there are two clusters on one layer's set of strips (indicative
665 of noise). Clusters are cut if the cluster size is lesser than three (which should not happen for
666 real events thanks to neighbour triggering), and if the cluster size is greater than 25. After
667 all the cuts on hits and clusters, roughly half as many muon tracks as triggers collected
668 remain.

669 The uncertainty in the y -coordinate could have been taken as the fitted cluster mean's
670 statistical uncertainty; however, after comparing the difference in cluster means for different
671 fitting algorithms in appendix A.2, 60 μm of uncertainty was assigned.

672 The coordinates of the avalanches' on all layers were used to reconstruct tracks in x and y
673 respectively. The tracks were then used to calculate characterization metrics like electrode
674 efficiency and spatial resolution, the details of which are discussed in [49].

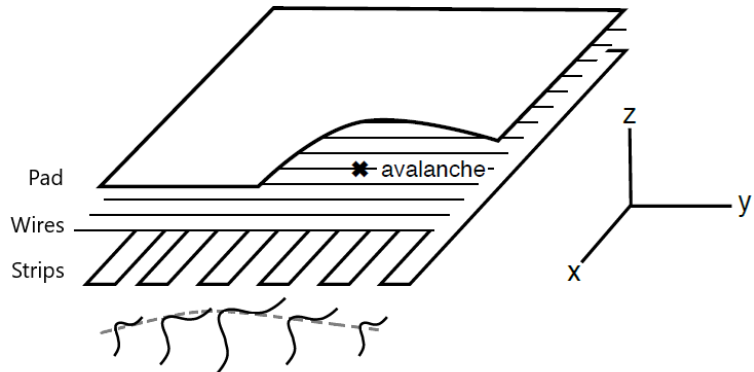


Figure 4.2: A sketch of an sTGC-like detector. The position of the avalanche is extracted from the wires and strips that picked up the avalanche signal. The signals on individual strips are sketched. Clustering was the processs of fitting a Gaussian to the peak value of the signals on individual contiguous strips, as is done in figure 4.3. In this work, the $x(y)$ -coordinate will always refer to the coordinate perpendicular to the wires (strips) [49, 46].

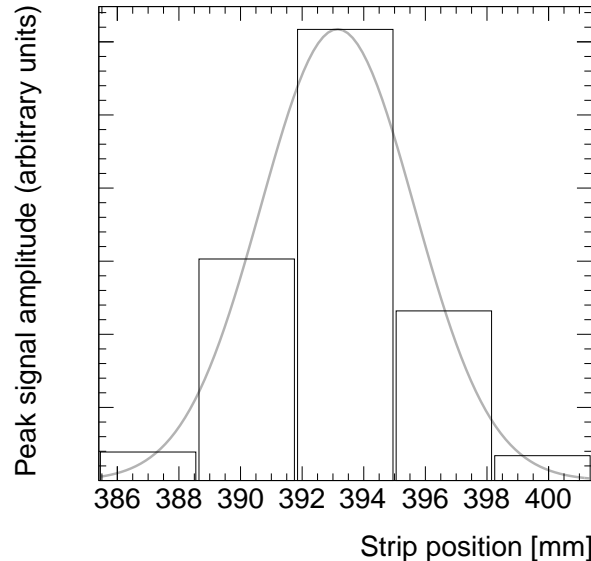


Figure 4.3: A sample cluster resulting from the current picked up on a group of strips after the passing of a muon (presumably). The grey curve is a Gaussian fit.

675 4.5 Measuring relative local offsets

676 The offset of a strip from its nominal position can be modeled as a passive transformation.
677 For each area of a strip layer, the local offset is the shift of the strip pattern in that area with
678 respect to the nominal geometry. Local offsets systematically change the set of strips nearest
679 to muons passing through the area. The data preparation software assumes that strips are
680 in their nominal positions, so the recorded muon y -position on layer i , y_i , is shifted opposite
681 to the layer's local offset, $d_{local,i}$, by

$$y_i = y_{nom,i} - d_{local,i}, \quad (4.1)$$

682 where $y_{nom,i}$ is the position of the muon that would have been recorded on layer i if there
683 was no local offset. Equation 4.1 ignores other factors that affect the cluster position, like
684 position resolution. With cosmics data, the local offset is unknown and there was no external
685 reference to measure $y_{nom,i}$. Therefore, only relative local offsets could be calculated.

686 The minimal relative coordinate system uses two reference or fixed layers [49]. The hits
687 on the two fixed layers were used to create tracks that can be interpolated or extrapolated
688 (polated) to the other two layers. The set of two fixed layers and the layer polated to are
689 referred to as a tracking combination. The residual of track i , Δ_i is defined as,

$$\Delta_i = y_i - y_{track,i}, \quad (4.2)$$

690 where $y_{track,i}$ is the polated track position. Track residuals are affected by the relative local
691 offset in the area of each layer's hit. As an example, in figure 4.4, the residual on layer
692 2 perhaps indicates that layer 2 is offset with respect to layers 1 and 4 in the area of the
693 track. Of course, a single track residual says nothing of the real relative local offset because
694 of the limited spatial resolution of the detectors and fake tracks caused by noise or delta
695 rays. However, the mean of residuals for all tracks in a region will be shifted systematically
696 by the local offsets between layers [49]. For a quadruplet with nominal geometry, the mean
697 of residuals should be zero in all regions and for all reference frames, unlike the example
698 regions in figure 4.5. The value of the mean of residuals is a measure of the relative local
699 offset of the layer with respect to the two fixed layers.

700 To study the relative local offsets, residual distributions across each strip layer of a quadruplet
701 for all tracking combinations were assembled and fitted. The residual distributions were
702 wider for tracking combinations where the extrapolation lever arm was largest, as in the
703 example distributions shown in figure 4.5. In general, residual means from distributions of
704 residuals with geometrically less favourable tracking combinations have larger statistical and
705 systematic uncertainties. The bin size of 200 μm for the distributions shown in figure 4.5 was

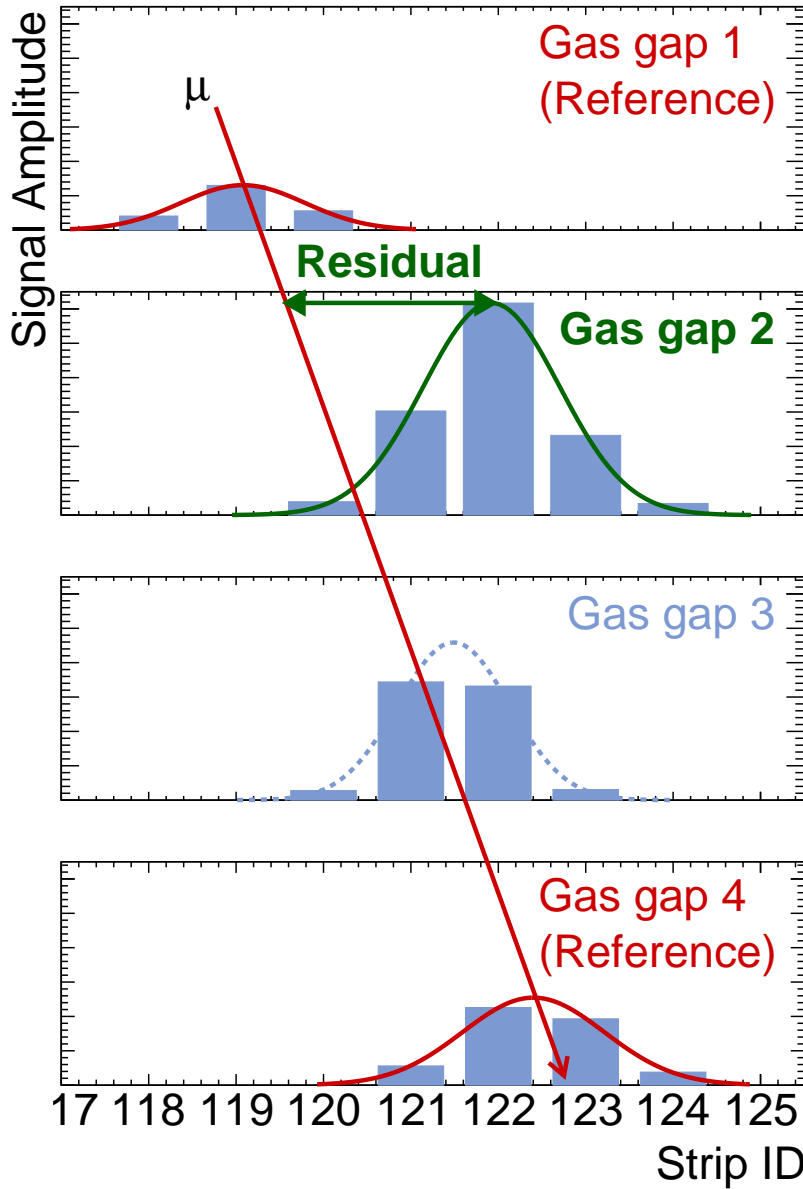
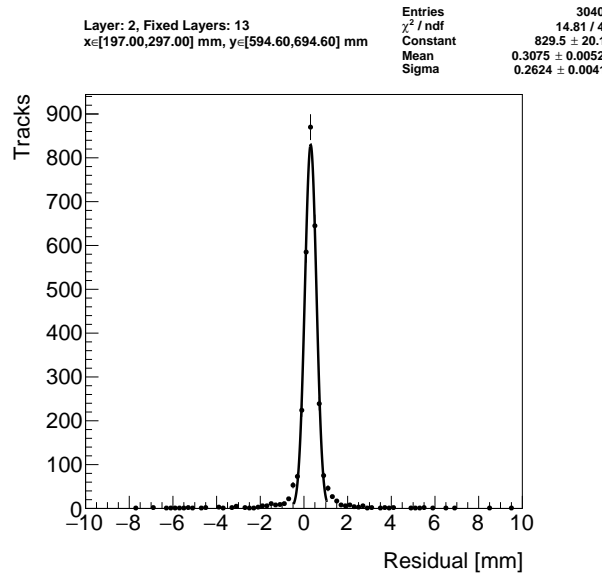
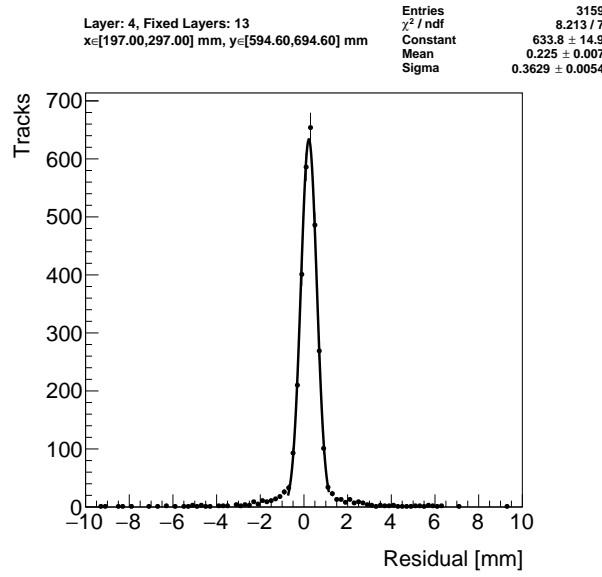


Figure 4.4: Representation of a muon event recorded by an sTGC. The clusters are fit with a Gaussian and the mean is taken as the hit position. A track is built from the chosen reference layers, 1 and 4, and the residual calculated on layer 2. The clusters come from a real muon, but their positions were modified to highlight the residual on layer 2.



(a) Tracks on layer 2, reference layers 1 and 3.



(b) Tracks on layer 4, reference layers 1 and 3.

Figure 4.5: Residual distribution in the region $x \in [197, 297]$, $y \in [594.6, 694.6]$ mm (100 mm by 100 mm area) for two different tracking combinations.

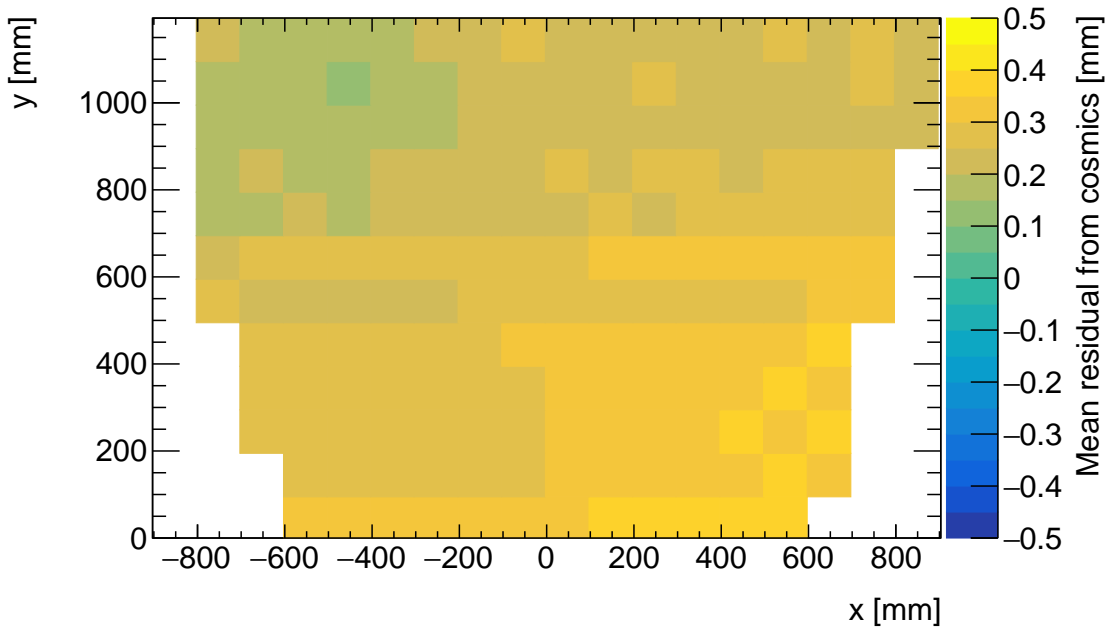
706 chosen based on the uncertainty on residuals calculated from tracks on layer 4 (1) built from
707 hits on layers 1 and 2 (3 and 4) given a cluster y -position uncertainty of $60 \mu\text{m}$ (appendix A.3),
708 since these tracks yield residuals with the largest uncertainties.

709 A gaussian fit was used to extract the mean of the residual distributions. Theoretically, a
710 double gaussian distribution is more apt, but for this analysis the gaussian fit was sufficient,
711 as discussed in appendix C.1.

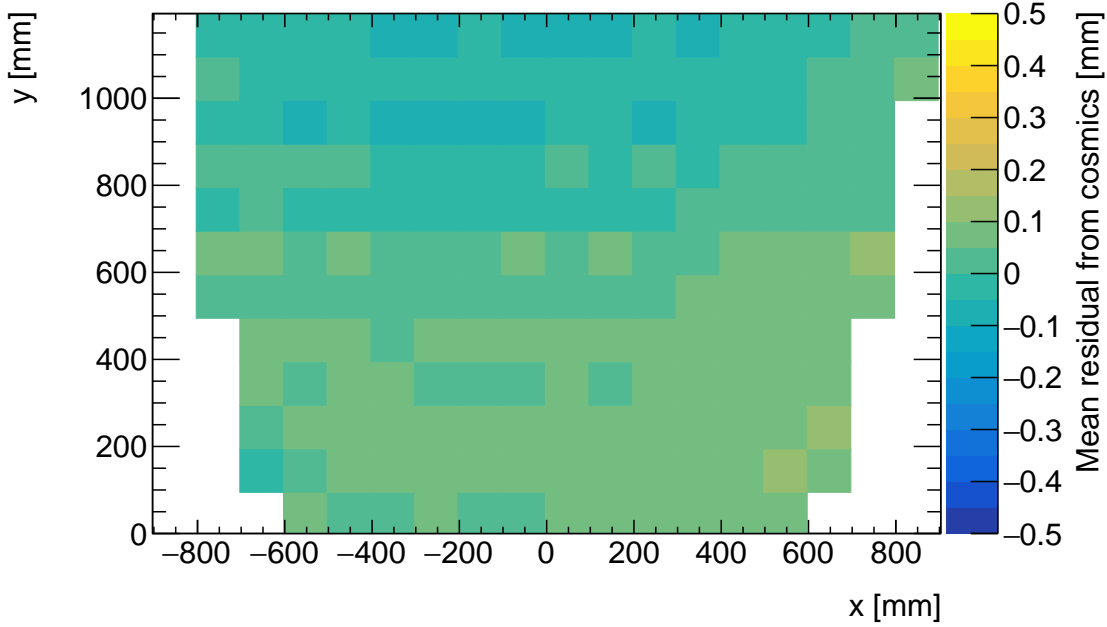
712 The area of the region of interest was 100 mm by 100 mm. The size balanced the amount of
713 tracks falling in the region of interest to give a small statistical uncertainty on the extracted
714 mean while being smaller than the order on which local offsets were expected to change
715 significantly. The change in local offsets over the surface of a layer can be modeled using
716 global alignment parameters. Using a base alignment model with a global offset and rotation
717 of each strip layer, “significantly” was defined by the distance in x that a large but possible
718 rotation of $1000 \mu\text{rad}$ would change the local offset by more than $50 \mu\text{m}$ – half the required
719 position resolution of the sTGCs [5].

720 4.6 Visualizing relative alignment between layers

721 The mean of residuals was plotted across entire strip layers for every tracking combination to
722 get a picture of the how relative local offsets change over the layers’ surface. Figure 4.6 shows
723 the mean of residuals on layer 2 with reference layers 1 and 3 for two different quadruplets,
724 referred to as quadruplet-1 and quadruplet-2, for 100 mm by 100 mm areas across the surface
725 of layer 2. To understand these plots, realize that the Gaussian mean of the distribution in
726 figure 4.5a is the entry in area bin $x \in [197, 297]$, $y \in [594.6, 694.6]$ mm in figure 4.6a.



(a) Mean of residuals of tracks on layer 2, reference layers 1 and 3, for quadruplet-1.



(b) Mean of residuals of tracks on layer 2, reference layers 1 and 3, for quadruplet-2.

Figure 4.6: Mean of residuals in each 100 mm by 100 mm bin over the area of the layer 2 cathode board. The entry in $x \in [197, 297]$, $y \in [594.6, 694.6]$ mm of figure 4.6a corresponds to the fitted Gaussian means in figures 4.5a. The mean of residuals is an estimate of the local offset of layer 2 with respect to layers 1 and 3.

727 Many of the residual means are non-zero and change smoothly over the layer, indicating
728 that there are relative local offsets stemming from misalignments between entire strip layers.
729 Given that the residual mean changes with x in figure 4.6a, there is likely a rotation of layer
730 2 with respect to layers 1 and 3 on quadruplet-1, combined with an offset of the entire layer.
731 The residual means are smaller in figure 4.6b indicating that quadruplet-2 is less misaligned
732 overall than quadruplet-1; however the relative local offsets range between $\pm 200 \mu\text{m}$ so they
733 are still significant considering the order on which the chambers must be sensitive to position,
734 $\sim 100 \mu\text{m}$.

735 4.7 Systematic uncertainty

736 The statistical uncertainty on the local residual means was typically around $10 - 20 \mu\text{m}$, and
737 appendix B shows that the analysis was not statistically limited by the number of triggers
738 collected for each quadruplet. The systematic uncertainties were more significant.
739 Systematic uncertainties were assigned per tracking combination as the RMS of the dis-
740 tribution of the difference in local residual means each calculated in a different way. For
741 example, the RMS associated with fitting the local residual distributions with a Gaussian or
742 double Gaussian is $25 \mu\text{m}$ for the geometrically least favourable tracking combinations. The
743 distribution is shown in appendix C.1. For geometrically similar tracking combinations (like:
744 tracks on layer 1 built from hits on layers 3 and 4, and tracks on layer 4 built from hits on
745 layers 1 and 2), the systematic uncertainty was assigned as the average RMS of both.
746 Other choices were: whether to use data collected at 2.9 kV or 3.1 kV (both are collected at
747 McGill); what cluster fitting algorithm to use; and whether or not to apply a differential non-
748 linearity (DNL) correction to the cluster y -positions. A systematic uncertainty was assigned
749 using the method above to account for the effect of each choice and quantify the robustness
750 of the mean of residuals. The reasons for each choice are listed below.
751 Data taken at 3.1 kV was used over 2.9 kV because the strip and wire tracking efficiency
752 increases with higher voltage [49] (appendix C.2).
753 The Minuit2 package [55] was used to fit clusters over Guo's method [56] because it provided
754 automatic statistical uncertainty estimates and is the standard fit algorithm of ROOT [53]
755 (appendix C.3).
756 The DNL correction was not applied because its effect on the residual means was negligible
757 (appendix C.4).
758 A summary of the systematic uncertainties assigned for each tracking combination is given
759 in table 4.1.

Tracking geometry	Residual distribution fit function (C.1)	Cosmics data collection voltage (C.2)	Cluster fit algorithm (C.3)	Apply DNL correction or not (C.4)	Total
Similar to layer 3, fixed layers 1, 2	0.01	0.04	0.02	0.01	0.05
Similar to layer 4, fixed layers 1, 2	0.03	0.01	0.03	0.01	0.10
Similar to layer 2, fixed layers 1, 3	0.01	0.02	0.01	0.000	0.03
Similar to layer 4, fixed layers 1, 3	0.01	0.04	0.01	0.01	0.04
Similar to layer 2, fixed layers 1, 4	0.01	0.04	0.01	0.01	0.04

Table 4.1: Systematic uncertainty assigned for each analysis option, detailed in appendix [C](#).

760 The uncertainty in each mean of residuals was assigned as the sum in quadrature of the sta-
761 tistical uncertainty in the mean and the appropriate systematic uncertainty for the tracking
762 combination.

763 4.8 Discussion

764 Cosmics data is being used to calculate relative alignment parameters using two other meth-
765 ods [49]. A cross-check of this analysis would be to compare their results; however the studies
766 in appendix C show that the mean cosmics residuals are robust, so the comparison was not
767 prioritized.

768 Given that the uncertainty in the residual means is lesser than or near to the order of the
769 required position resolution of the sTGCs ($100 \mu\text{m}$ [5]) they are relevant input for alignment
770 studies.

771 The relative local offsets as calculated from the mean of residual distributions provide a
772 complete picture of the relative alignment between detectors planes. In fact, cosmic muon
773 testing is the only characterization technique where the entire surface of quadruplet layers
774 can be probed since muons hits are distributed almost uniformly; the CMM [8] and x-ray
775 methods [9] depend on measurements at reference points, and test beams only have a limited
776 beam spot [6]. By looking at 2D-histograms of residual means like figure 4.6 for all tracking
777 combinations, it is easy to identify quadruplets that suffer large relative misalignment since
778 many residual means differ significantly from zero. Moreover, the pattern in the relative
779 local offsets can be used to motivate a physical interpretation of misalignments. The relative
780 local offsets can be used as a reference, cross check, or input in other alignment studies.

781 Relative local offsets cannot be used to position strips in the absolute ATLAS coordinate
782 system because there was no external reference to measure positions on all layers with re-
783 spect to. The lack of external reference means that there is not enough information to unfold
784 relative local offsets into absolute local offsets (with respect to the nominal quadruplet ge-
785 ometry). As an example, assuming that the residual on layer 2 in figure 4.4 is representative
786 of the relative local offset, the residual on layer 2 could be caused by the strips on layer 2
787 being misaligned from nominal, but it could also be caused by strips on layers 1 and 4 being
788 offset from nominal while the strips on layer 2 are in their nominal positions! Any number
789 of combinations of local offsets on layers 1, 2 and 4 could produce the residual on layer 2.
790 Absolute local offsets must be calculated another way.

791 **Chapter 5**

792 **Using x-rays to measure relative strip
793 position offsets**

794 Local offset measurements were done with the x-ray method. The reader is referred to the
795 paper describing the x-ray method [9], although some minor changes have been made to the
796 experimental setup since it was written. The experimental setup described here is current
797 and was used to collect the data presented in this thesis.

798 **5.1 Experimental setup**

799 The x-ray tests were performed after the quadruplets arrived at CERN, were assembled into
800 wedges, and alignment platforms installed. Essentially, an x-ray gun was attached to one
801 of the alignment platforms glued to the surface of the wedge and the x-ray beam profile
802 recorded by the strips.

803 The wedges were installed on carts that could rotate their surface to a horizontal position. A
804 mounting platform was installed on top of the alignment platform using a three-ball mount.
805 The x-ray gun used was an [Amptek Mini-X tube](#). The gun was placed in a brass holder
806 with built-in 2 mm collimator and 280 μm copper filter. The holder was mounted on one
807 of five positions on the mounting platform, as shown in figure 5.1. Gun positions were
808 chosen to avoid wire support structures in the sTGCs that reduce hit efficiency [49] and
809 boundaries between sets of strips read out by two different ASICs that could each have
810 different thresholds.

811 As with cosmics data collection, each sTGC also needed gas and high voltage to operate.

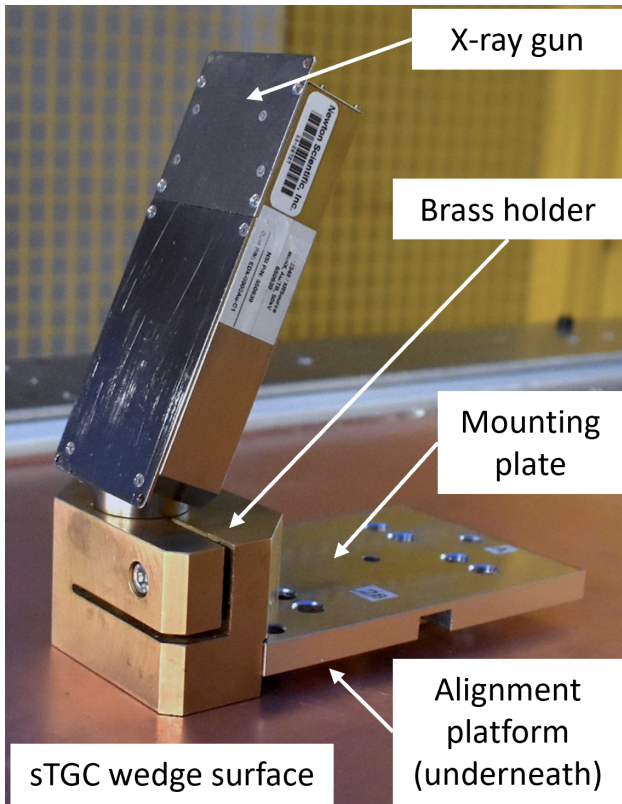


Figure 5.1: The x-ray gun mounted to the alignment platform on the surface of the wedge.
Adapted from [9].

812 Each layer was operated at 2.925 kV with high voltage from a NIM crate. The chambers
813 were flushed with CO₂ before and during data collection.
814 The gun produced x-rays with energies under 40 keV with peaks in the 7-15 keV range. The
815 x-rays mostly interacted with the wedge's copper electrodes and gold-plated tungsten wires
816 via the photo effect. The resulting photoelectrons caused ionization avalanches that were
817 picked up by the strips.

818 5.2 Data acquisition

819 A different version of the same front end electronics, but the same ASIC, as used in cosmics
820 testing were used for the x-ray testing to amplify the data and measure the peak signal
821 amplitude. Data was collected for two minutes per gun position with random triggers. A
822 trigger recorded all signals above threshold. Pad and wire data was not recorded.

823 5.3 Data preparation

824 Like with cosmics analysis, a default pedestal is subtracted from the signal peak amplitude
825 on each electrode.
826 Clusters are defined as groups of contiguous strip hits collected within 75 ns. The peak signal
827 amplitude of each electrode in a cluster is fit with a Gaussian, and the mean of the Gaussian
828 is taken as the cluster position. Cluster positions are corrected for DNL (see definition in
829 appendix C.4). Only clusters composed of hits on 3-5 strips were used in the x-ray analysis.
830 Clusters with signal on more than 5 strips were cut because they were most likely caused by
831 photoelectrons ejected with enough energy to be δ -rays.
832 The x-ray analysis diverges entirely from the cosmics analysis algorithm here because the
833 x-rays do not leave tracks. The signals picked up by the strips are from photoelectrons
834 liberated from the metals of the sTGCs, which only travel through one gas volume and are
835 ejected at all angles. Instead of creating tracks, the cluster position distribution on each
836 layer is used to define the beam profile. A typical beam profile is shown in figure 5.2.

837 5.4 Measuring local offsets

838 The mean of the cluster position distribution is taken as the x-ray beam profile center.
839 The expected center is calculated assuming a wedge with nominal geometry given the gun



Figure 5.2: Distribution of x-ray cluster mean positions after the analysis cuts and corrections. The strip cluster multiplicity, m , was limited to 3, 4 and 5. The red curve is a Gaussian fit of the distribution and the pink dashed lines denote the edges of the strips [9].

position, corrected for: the geometry of the brass holder, the positioning and angle of the alignment platforms and the beam angle. The difference between the expected and reconstructed beam profile center is a measure of the local offset. Applying the logic of equation 4.1 to the beam profile, the Gaussian mean of cluster positions on the given layer acts as the recorded position, y_i , the expected center is $y_{nom,i}$ and the local offset is $d_{local,i}$ as before, where i denotes the layer. Since the position of the alignment platforms will be monitored by the alignment system in ATLAS [5], the position of the strips that should have been at the gun position are shifted by $d_{local,i}$ and so are known in the ATLAS coordinate system for every position where x-ray data was taken.

The x-ray working group accepted an uncertainty of 120 μm on the beam profile centers. The largest uncertainty comes from the effect of the gun angle, which proved difficult to measure and correct for.

The local offsets are not presented here as the author did not conduct this work. However, the author used the local offsets to calculate relative local offsets.

5.5 Measuring relative local offsets

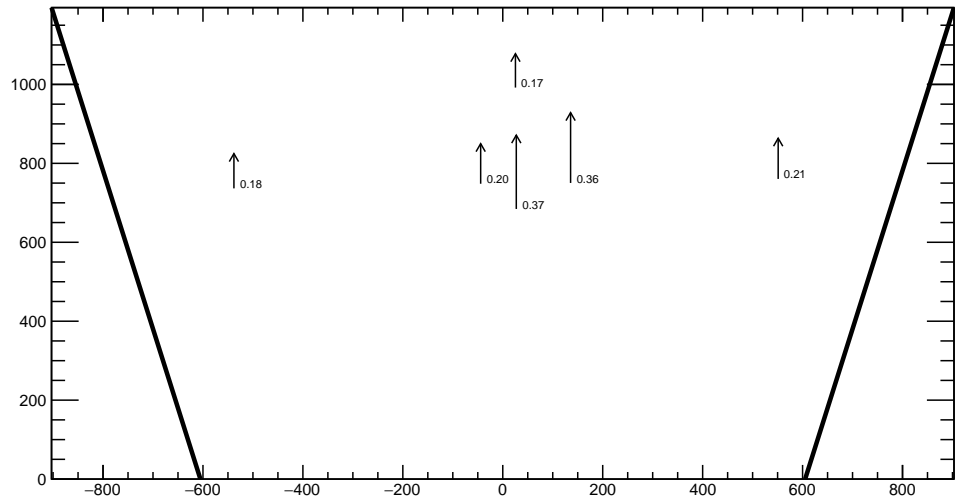
The x-ray local offsets were shown to be correlated with the local offsets calculated from the CMM data, but the CMM data does not include the effect of inter-layer misalignments so the degree of correlation measurable was limited. Cosmics data is affected by inter-layer misalignments. Since the local offsets for x-rays and cosmics data are measured in different coordinate systems, they cannot be compared directly. Bringing the cosmics relative local offsets into an absolute coordinate system is impossible; however, the x-ray local offsets can be brought into a relative coordinate system.

The measured x-ray beam profile centers were systematically affected by local offsets in the same way as the mean cosmics residuals, as modeled by equation 4.1. Therefore, if a 2-layer track is built from the beam profile centers on each layer and the residual calculated on a third layer, that residual should match the local mean cosmics residual. The residual is the difference between the beam profile center on the layer of interest and the polated track position from the beam profile centers recorded on the two fixed layers. The beam profile center on the layer of interest acts as y_i and the polated track position acts as $y_{track,i}$ in equation 4.2.

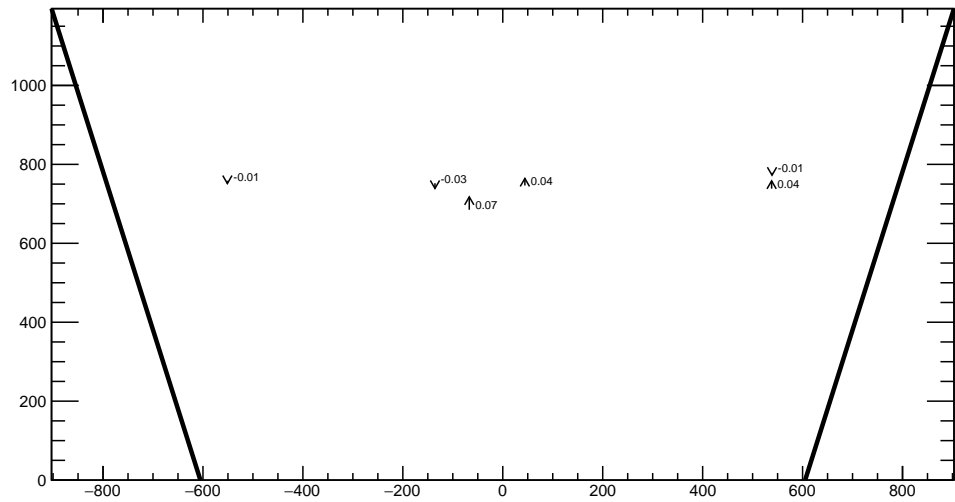
The built track is not an actual track of the x-ray beam. A beam profile center is actually the Gaussian mean of all selected mean cluster positions recorded during the x-ray data taking period, not a single hit of a track. Building an “abstract” track was necessary because

873 the x-rays cause signal in the chamber via the photoeffect so there were not individual “x-
874 ray tracks” to record. In fact the x-ray data could be collected separately for each layer.
875 Nonetheless, since the effect of local offsets on the beam profile centers was the same as their
876 effect on the recorded cosmics cluster positions the difference in algorithm between x-ray
877 and cosmics analysis was allowed.

878 For each x-ray survey position, the x-ray residual was calculated for all possible tracking
879 combinations (which required an x-ray beam profile on at least three layers). The x-ray
880 residuals on layer 2 calculated from the beam profile centers recorded on layers 1 and 3
881 are represented as arrows in figure 5.3 as arrows for quadruplet-1 and quadruplet-2. For
882 quadruplet-1, a negative offset at all x-ray survey positions is clear.



(a) Quadruplet-1 x-ray residuals on layer 2, reference layers 1 and 3.



(b) Quadruplet-2 x-ray residuals on layer 2, reference layers 1 and 3.

Figure 5.3: The x-ray residuals on layer 2 calculated from the beam profile centers recorded on layers 1 and 3 for quadruplet-1 and quadruplet-2. The arrows originate from the expected position of the beam profile center assuming a nominal geometry, and the lengths are proportional to the calculated x-ray residuals. The tip of the arrow represents where the recorded hit was with respect to where it should have been recorded nominally. The value of the x-ray residuals are annotated in millimeters and have an uncertainty of ± 0.15 mm.

883 The uncertainty on the x-ray residuals was the error propagated through the tracking, taking
884 an uncertainty of 120 μm on each beam profile center. The uncertainty on the x-ray residuals
885 ranged from 0.15 mm to 0.4 mm from the most to least geometrically-favourable tracking
886 combination. There is no discernible pattern to the x-ray residuals on quadruplet-2 because
887 they are smaller than the uncertainty. The x-ray residual uncertainties are significantly
888 larger than the uncertainties on the relative local offsets calculated with cosmics data.

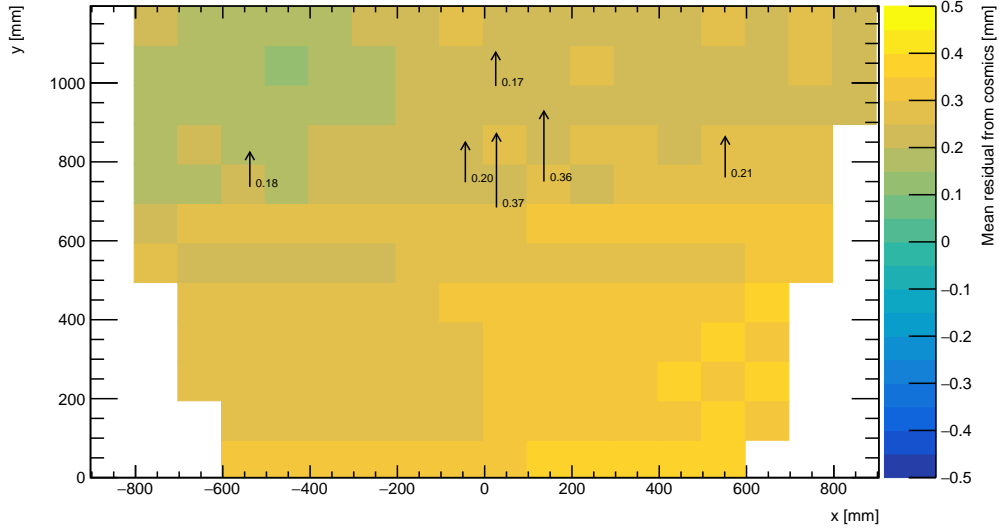
889 **Chapter 6**

890 **Comparing cosmic muon and x-ray
891 relative strip position offsets**

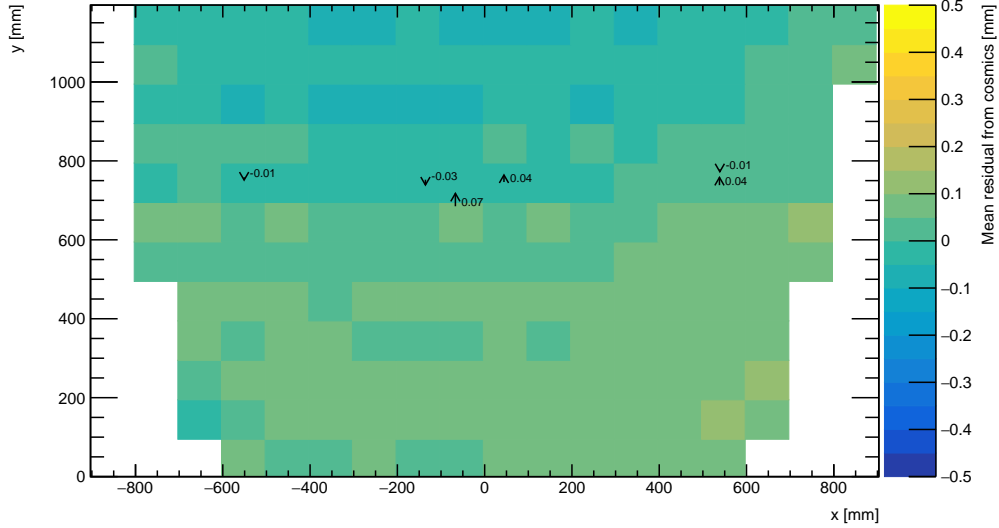
892 The goal was to validate the local offsets extracted from the x-ray data with cosmics data.
893 The complication was that the x-ray dataset provided absolute local offsets while the cosmics
894 dataset provided relative local offsets, which could not be compared directly. The solution
895 was to use the x-ray local offsets to calculate relative local offsets. The x-ray relative local
896 offset is the x-ray residual reconstructed from an abstract track using the beam profile
897 centers on each layer as the track hits. The cosmics relative local offset was taken as the
898 Gaussian mean of muon track residuals in a 100 mm by 100 mm area, referred to as the
899 the mean cosmics residual. Relative local offsets of each type calculated using the same
900 reference layers are compared for each area where x-ray data is available. The results of the
901 comparison are presented here.

902 **6.1 Assessing correlation**

903 The 2D visualizations of the mean cosmics and x-ray residuals for tracks on layer 2 with
904 reference layers 1 and 3 on quadruplet-1 and quadruplet-2 are shown in figure 6.1. Figure 6.1
905 is a superposition of figures 4.6 and 5.3.



(a) Quadruplet-1 residuals of tracks on layer 2, reference layers 1 and 3.



(b) Quadruplet-2 residuals of tracks on layer 2, reference layers 1 and 3.

Figure 6.1: The mean cosmics residuals are shown using colour. The x-ray residuals available at nominal gun positions are drawn as arrows and the value of the residual annotated in millimeters with uncertainty ± 0.15 mm. The length of the arrows is 500 times the value of the x-ray residual, scaled for visibility. These plots are a superposition of figures 4.6 and 5.3.

906 Figure 6.1a shows that for quadruplet-1 the x-ray residuals are of the same sign and order as
907 the mean cosmics residuals, as can be seen by comparing the the annotated value of the x-ray
908 residual to the mean cosmics residual represented by colour; quadruplet-1's mean cosmics
909 and x-ray residuals are correlated to some degree. For quadruplet-2, the x-ray residuals
910 are of the right order compared to the mean cosmics residuals, but the correlation is less
911 apparent. While x-ray residuals do not reveal a pattern across the layer's surface, the mean
912 cosmics residuals show a structure to the relative local offsets since they vary smoothly over
913 the surface of layer 2.

914 The comparison of mean cosmics and x-ray residuals was done for several quadruplets for
915 all tracking combinations (not just layer 2 residuals calculated with fixed layers 1 and 3 like
916 in figure 6.1). Scatter plots of the x-ray and mean cosmics residuals on quadruplet-1 and
917 -2 for all tracking combinations shown in figures 6.2 and 6.3 reveal the degree of correlation
918 between the datasets. In the correlation plots, each rectangle is centered on the value of a
919 mean cosmics and x-ray residual pair calculated with a given tracking combination for every
920 gun position where data is available; the height and width of the squares are the uncertainty
921 in the mean cosmics and x-ray residuals respectively. Note that in the scatter plots, the
922 regions of interest where cosmics tracks are included in the calculation of mean of residuals
923 are exactly centered on the nominal x-ray beam position, unlike in figure 6.1.

924 The fitted slope and offset in figure 6.2 show that the two quadruplet-1 datasets are cor-
925 related. The large uncertainty on the x-ray residuals set a limit on the sensitivity of the
926 analysis, for if the absolute value of the x-ray residuals of a quadruplet were smaller than
927 the x-ray residual uncertainties, no conclusion about the correlation could be drawn, like
928 for quadruplet-2 (figure 6.3). This result is reflected in the small x-ray residuals shown in
929 figure 6.1b that do not reveal a pattern in the relative local offsets across the surface of layer
930 2. However, figure 6.3 shows that the x-ray and mean cosmics residuals are centered around
931 zero, as is expected for a quadruplet with small relative misalignments between layers.

932 There are three patterns in the residuals on the scatter plot explained by geometry. First,
933 for both datasets the uncertainty in the extrapolated track residuals were larger than the
934 interpolated track residuals because of the extrapolation lever arm. For the x-ray residuals,
935 the effect of the lever arm on the uncertainty was direct since the residual was calculated from
936 a single abstract track; for the mean cosmics residuals it was the widening of the residual
937 distribution due to the extrapolation lever arm that increased the uncertainty in the fitted
938 mean of residuals. Second, residuals calculated through extrapolation tend to be larger
939 because the extrapolation lever arm can produce more extreme values of the track position
940 on the layer of interest. Third, the points in figure 6.2 are geometrically correlated (e.g.
941 they seem to be roughly mirrored around the origin). This is expected since the residuals
942 calculated using a given set of three layers should be geometrically correlated by the local

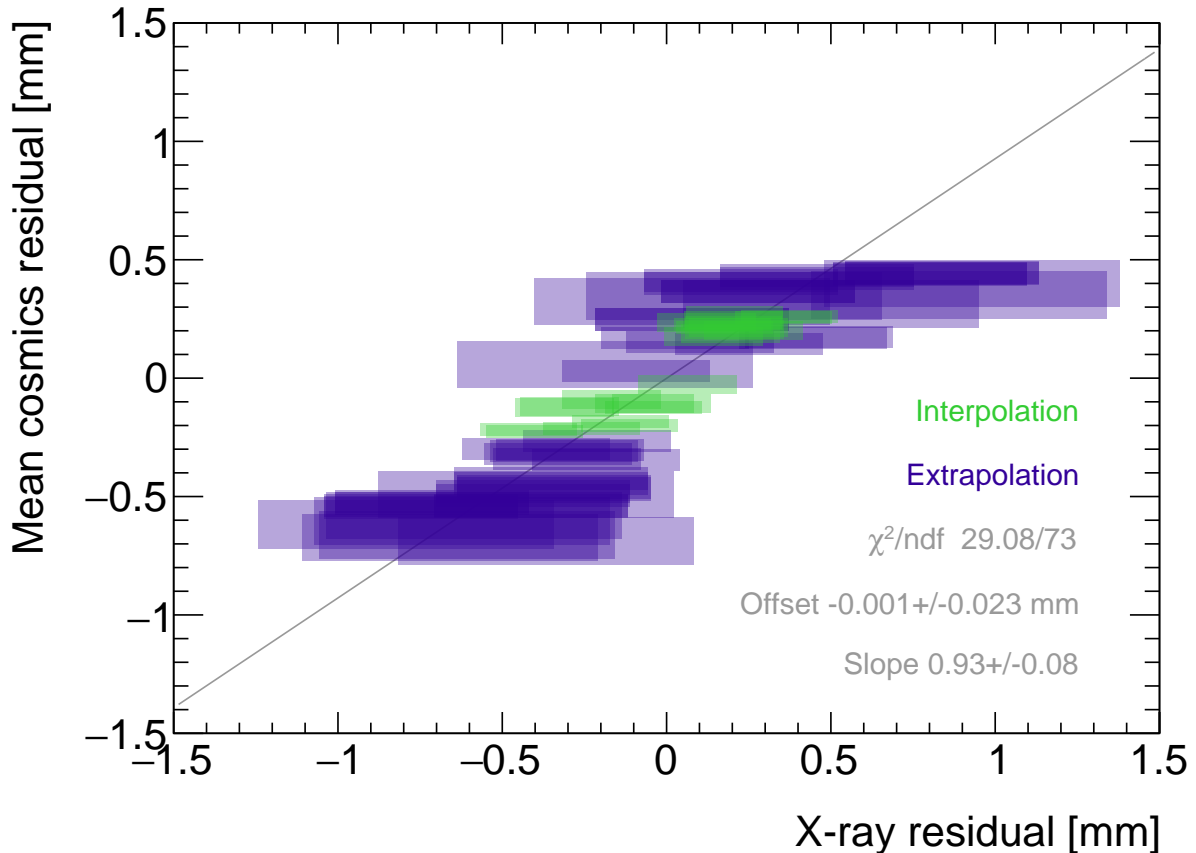


Figure 6.2: Correlation plot between x-ray and mean cosmics residuals for all tracking combinations for quadruplet-1. Each rectangle is centered on an x-ray and mean cosmics residual pair calculated at a given gun position and for a certain tracking combination. The width of the rectangles in x and y are the uncertainty in the x-ray and mean cosmics residual respectively. A printer-friendly version of this plot is available in appendix D.

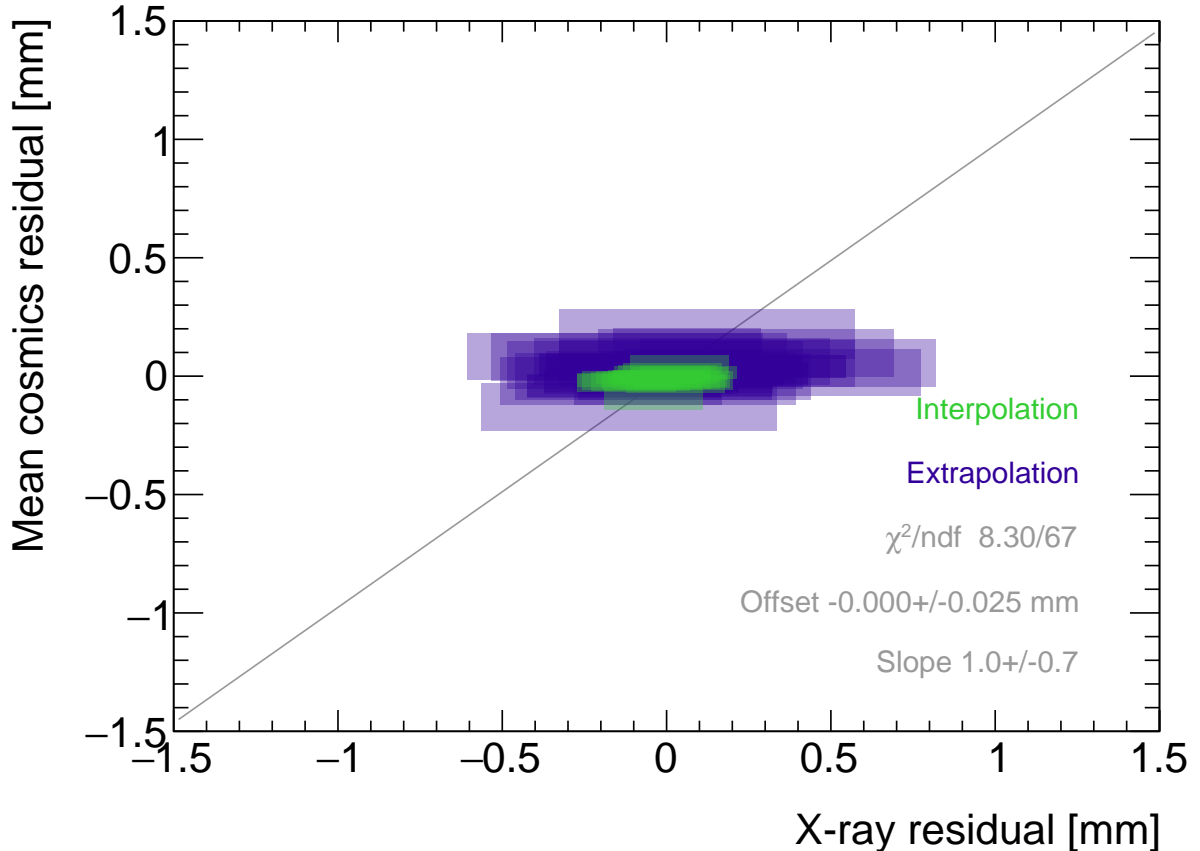


Figure 6.3: Correlation plot between x-ray and mean cosmics residuals for all tracking combinations for quadruplet 2. Each rectangle is centered on an x-ray and mean cosmics residual pair calculated at a given gun position and for a certain tracking combination. The width of the rectangles in x and y are the uncertainty in the x-ray and mean cosmics residual respectively. A printer-friendly version of this plot is available in appendix D.

943 offsets on the fixed layers and the layer of interest (the $d_{local,i}$ on each layer as defined in
944 equation 4.1).

945 6.2 Discussion

946 Several quadruplets were tested for each quadruplet construction geometry built in Canada.
947 Each quadruplet fell into one of the two categories: residuals large enough to see a correlation,
948 or residuals too small to see a correlation. Since the x-ray and mean cosmics residuals
949 were measures of the relative local offsets between the layer and the two reference layers,
950 quadruplets with the largest relative misalignments had the largest range of residuals. the
951 correlation plots were an easy visual way to identify quadruplets with large relative misalign-
952 ments.

953 The most significant limit on measuring the degree of correlation between the x-ray and
954 mean cosmics residuals was the uncertainty on the x-ray residuals, which stemmed from
955 the systematic uncertainty of 120 μm in the x-ray beam profile centers used to build the
956 abstract tracks. For example, in figure 6.3 the uncertainty in the x-ray residuals makes
957 detecting correlation impossible. The x-ray method was limited primarily by the systematic
958 uncertainties in the relative alignment of the platforms and the gun, especially the gun angle.

959 The analysis of certain quadruplets was limited by the availability of data. Sometimes,
960 less than three layers were surveyed for a given x-ray gun position so no residuals could
961 be calculated. Too few x-ray residuals prevented the analysis from detecting a significant
962 correlation, should it even be measurable. Often, the analysis of smaller quadruplets (placed
963 innermost on the wheel) suffered as a result because they had fewer alignment platforms, and
964 hence gun positions, on their surfaces. The analysis was also limited to certain quadruplets.
965 The wedges constructed the earliest (typically small wedges) were surveyed when the x-ray
966 method was still being designed and so have limited x-ray residuals calculated from beam
967 profiles of lower quality. In addition, not all cosmic muon test sites had enough front end
968 electronics to collect data on three layers simultaneously, which is the minimum required to
969 be able to calculate residuals.

970 Nonetheless, the comparison of x-ray and cosmics residuals was really to confirm the x-ray
971 method's ability to measure local offsets with an independent dataset. The x-ray local offsets
972 allow the calculation of relative local offsets that have been correlated to the cosmics relative
973 local offsets. Therefore, the analysis of quadruplets with relative local offsets large enough
974 to detect a correlation validates the x-ray method's ability to measure local offsets.

975 The potential of using relative local offsets calculated from cosmics data to study relative
976 alignment between sTGC layers stands on its own. For example, although the x-ray relative

977 local offsets of quadruplet-2 in figure 6.1b do not reveal a pattern, the variation in the cosmics
978 relative local offsets do. Identifying the pattern is possible because mean cosmics residuals
979 can be calculated across the entire area and are sensitive to smaller relative local offsets since
980 their uncertainty is significantly smaller.

981 The advantage of the x-ray dataset over the cosmics dataset is that absolute local offsets
982 are measurable thanks to the reference frame provided by the alignment platforms. This is
983 required to measure the position of strips in the ATLAS coordinate system to satisfy the
984 NSWs' precision tracking goals. The x-ray local offsets are being used to build an alignment
985 model of strips in each quadruplet. It is compelling to imagine using the cosmics relative
986 local offsets to improve the model considering their precision and ability to capture effects
987 across the entire area of the quadruplet.

988 **Chapter 7**

989 **Outlook and summary**

990 The cosmic muon dataset was used to independently confirm the absolute local offsets mea-
991 sured by the x-ray method. The x-ray offsets are being used to complete the sTGC alignment
992 scheme of the NSWs: the NSW alignment system monitors the position of alignment plat-
993 forms on the surface of sTGC wedges, and the x-ray measurements provide the offsets of
994 the strip pattern with respect to each alignment platform. The continuation of this anal-
995 ysis is detailed next (section 7.1) before summarizing and considering the larger context
996 (section 7.2).

997 **7.1 Outlook**

998 Next all quadruplets with suitable cosmics and x-ray data should be surveyed to flag anom-
999 lous quadruplets (as a first step). If a quadruplet's correlation plot like figure 6.2 or 6.3
1000 reveals an unexpected correlation or has a large scatter, it would indicate an issue with ei-
1001 ther the cosmics or x-ray data collection to be investigated further. The uncertainty in each
1002 set of tracking points would inform the interpretation of the anomaly. Then, the quality of
1003 the correlation should be evaluated over all quadruplets instead of individually.

1004 For now, the correlation for the individual quadruplets tested support the use of the x-ray
1005 data to build an alignment model [9]. Work on creating an alignment model is ongoing.
1006 Currently, the algorithm compares the y -position of a local group of strips at each x-ray gun
1007 position as measured by the x-ray and CMM methods in a fit to extract a global slope (m)

1008 and offset (b) per layer, i , where the χ^2 is given by equation 7.1.

$$\chi^2 = \frac{[dy_{cmm,corr} - dy_{xray}]^2}{\delta dy_{xray}^2 + \delta dy_{cmm,corr}^2}, \quad (7.1)$$

1009

$$dy_{cmm,corr} = y_{cmm} + b_i + m_i x - y_{nom} \quad (7.2)$$

1010 Here, dy refers to the corrected CMM and x-ray local offsets, and δdy refers to their re-
1011 spective uncertainties. The CMM measurements were taken before the cathode boards were
1012 assembled into quadruplets, so alignment parameters for the given layer were extracted from
1013 the χ^2 fit by stepping the corrected CMM y -position towards the x-ray y -position by adjust-
1014 ing the layer's slope and offset parameters. The plan is that the alignment parameters will
1015 be provided to the ATLAS experiment's offline software to reconstruct muon tracks from the
1016 NSWs' sTGCs. The large uncertainty on the x-ray local offsets (120 μm) and the sparseness
1017 of the measurements means that including input from other characterization datasets could
1018 reduce the uncertainty on the alignment model parameters.

1019 The uncertainty in the mean cosmics residuals was smaller than the desired position reso-
1020 lution of the sTGCs, so they provide relevant information about strip positions. Moreover,
1021 they can be calculated over the entire area of the quadruplet instead of at specific posi-
1022 tions. It would be great to use the cosmics residuals as input to calculate and reduce the
1023 uncertainty on the alignment parameters. Since mean cosmics residuals can only provide
1024 relative alignment information, one idea would be to use them to constrain the fit of the
1025 alignment parameters. In this case, the alignment parameters would need to be fitted on all
1026 layers at once, and the shifting y -positions on each layer forced to create an abstracted track
1027 residual equal to the local mean cosmics residual (within uncertainty) for each x-ray point.
1028 Or, instead of constraining the fit, it could be penalized if the resulting parameters do not
1029 result in abstracted track residuals equal to the mean cosmics residuals within uncertainty.
1030 Some work on using the three datasets at once in a fit has been started.

1031 7.2 Summary

1032 The LHC [1] will be at the energy frontier of particle physics for at least the next decade,
1033 making it a unique tool with which to study particle physics. With the HL-LHC [2], high
1034 statistics on rare particle physics processes will enable more precise measurements of param-
1035 eters of the Standard Model and increase the sensitivity to signatures of physics beyond the
1036 Standard Model [4]. To capitalize on the increased collision rate, the NSWs of the ATLAS
1037 experiment must be replaced to keep the triggering and tracking performance [5].

1038 Small-strip thin gap chambers are gas ionization chambers optimized for a high rate envi-
1039 ronment [5]. Using the pad electrodes to define a region of interest makes it possible to get
1040 track segments of ~ 1 mrad angular resolution quickly, which will be used as input to check
1041 if a collision originated from the interaction point and should be triggered on or not [5, 7].
1042 sTGCs are also able to provide better than $100 \mu\text{m}$ position resolution on each detector plane
1043 to fulfill precision offline tracking requirements [6].

1044 Ultimately, the positions of the sTGC strip electrodes need to be known in ATLAS to within
1045 $\sim 100 \mu\text{m}$ so that they can deliver the required position resolution. The ATLAS alignment
1046 system will position alignment platforms on the surface of the sTGC wedge, and an alignment
1047 model will be used to position the strips with respect to the alignment platforms [5]. Input
1048 to the alignment model comes from the datasets used to characterize the quadruplets. The
1049 x-ray method [9] is used to measure offsets of strips from their nominal position to achieve
1050 this goal. The alignment model could be built on x-ray data alone, but the sparseness of
1051 and large uncertainty on the local offsets mean that the alignment model could benefit from
1052 more input. Comparing the x-ray offsets to the CMM data [8] allows the effect of inter-layer
1053 misalignments to be isolated and increases the input to the alignment model.

1054 The cosmics dataset was used to confirm the local offsets measured with the x-ray gun. It
1055 provides relative local offsets between sTGC strip layers. The 2D visualizations of relative
1056 local offsets allow personnel to quickly identify areas of misaligned strips and make hypothe-
1057 ses of the physical origin of those misalignments. The correlation seen between the x-ray and
1058 cosmics relative local offsets in quadruplets with large relative misalignments both confirms
1059 the validity of the x-ray local offsets and again is a quick way to identify quadruplets with
1060 large misalignments. Moreover, the mean of track residuals in an area is a robust estimation
1061 of the relative local offset, as shown by the estimation of systematic uncertainties; the relative
1062 local offsets for all two-fixed layer reference frames do not change by more than $100 \mu\text{m}$ given
1063 variation in data collection conditions and analysis algorithms. The cosmics relative local
1064 offsets are therefore relevant input for alignment studies and could improve the alignment
1065 model that will position each strip.

1066 Achieving the required position resolution on each layer of the NSWs in the particle track
1067 bending plane achieves the design momentum resolution for muons ejected towards the end-
1068 caps of ATLAS. Muons are important signatures of electroweak and Higgs sector events
1069 of interest for the ATLAS Collaboration’s future physics goals [5]. Being the second of two
1070 tracking technologies on the NSWs, an effective alignment model of sTGC quadruplets layers
1071 is a necessary part of making the NSWs redundant for 10 or more years of recording collisions
1072 in the High Luminosity era of the LHC.

1073 References

- 1074 [1] L Evans and P Bryant. LHC Machine. *Journal of Instrumentation*, 3(S08001), 2008.
- 1075 [2] G Apollinari, I Bejar Alonso, O Bruning, P Fessia, M Lamont, L Rossi, and L Tavian.
1076 High-Luminosity Large Hadron Collider (HL-LHC) Technical Design Report V. 0.1.
1077 Technical report, CERN, Geneva, September 2017.
- 1078 [3] The ATLAS Collaboration. The ATLAS Experiment at the CERN Large Hadron Col-
1079 linder. *Journal of Instrumentation*, 3(08):S08003, 2008.
- 1080 [4] A Dainese et al. The physics potential of HL-LHC. In *Input to the European Particle
1081 Physics Strategy Update*, November 2018.
- 1082 [5] T Kawamoto, S Vlachos, L Pontecorvo, J Dubbert, G Mikenberg, P Iengo, C Dallapic-
1083 colà, C Amelung, L Levinson, R Richter, and D Lellouch. New Small Wheel Technical
1084 Design Report. Technical report, Jun 2013. ATLAS New Small Wheel Technical Design
1085 Report.
- 1086 [6] Angel Abusleme et al. Performance of a Full-Size Small-Strip Thin Gap Chamber Pro-
1087 totype for the ATLAS New Small Wheel Muon Upgrade. *Nuclear Instruments and
1088 Methods in Physics Research Section A: Accelerators, Spectrometers, Detectors and As-
1089 sociated Equipment*, 817:85–92, May 2016. arXiv: 1509.06329.
- 1090 [7] E. Perez Codina. Small-strip Thin Gap Chambers for the muon spectrometer upgrade of
1091 the ATLAS experiment. *Nuclear Instruments and Methods in Physics Research Section
1092 A: Accelerators, Spectrometers, Detectors and Associated Equipment*, 824:559–561, July
1093 2016.
- 1094 [8] Evan Michael Carlson. *Results of the 2018 ATLAS sTGC test beam and internal strip
1095 alignment of sTGC detectors*. Thesis, University of Victoria, Victoria, Canada, 2019.
1096 Accepted: 2019-07-16T17:20:40Z.

- 1097 [9] B. Lefebvre. Precision survey of the readout strips of small-strip Thin Gap Chambers
1098 using X-rays for the muon spectrometer upgrade of the ATLAS experiment. *Journal of*
1099 *Instrumentation*, 15(07):C07013–C07013, July 2020.
- 1100 [10] David J. Griffiths. *Introduction to elementary particles*. Physics textbook. Wiley-VCH,
1101 Weinheim, Germany, 2., rev. ed., 5. reprint edition, 2011.
- 1102 [11] Michael Edward Peskin and Daniel V. Schroeder. *An introduction to quantum field*
1103 *theory*. Addison-Wesley Pub. Co, Reading, Massachusetts, 1995.
- 1104 [12] P.A. Zyla et al. Review of Particle Physics. *PTEP*, 2020(8):083C01, 2020.
- 1105 [13] K. Kodama et al. Detection and analysis of tau neutrino interactions in DONUT
1106 emulsion target. *Nucl. Instrum. Meth. A*, 493:45–66, 2002.
- 1107 [14] David Galbraith and Carsten Burgard. UX: Standard Model of the Standard Model,
1108 November 2013.
- 1109 [15] Carlos A. Bertulani. *Nuclear physics in a nutshell*. In a nutshell. Princeton University
1110 Press, Princeton, N.J, 2007. OCLC: ocm85690422.
- 1111 [16] Bradley W. Carroll and Dale A. Ostlie. *An introduction to modern astrophysics*. Pearson
1112 Addison-Wesley, San Francisco, 2nd ed edition, 2007. OCLC: ocm69020924.
- 1113 [17] Mirko Boezio and Emiliano Mocchiutti. Chemical composition of galactic cosmic rays
1114 with space experiments. *Astroparticle Physics*, 39-40:95–108, December 2012.
- 1115 [18] Carlos Muñoz. Dark matter detection in the light of recent experimental results. *Inter-*
1116 *national Journal of Modern Physics A*, 19(19):3093–3169, July 2004.
- 1117 [19] B. Aharmim et al. Combined analysis of all three phases of solar neutrino data from
1118 the sudbury neutrino observatory. *Phys. Rev. C*, 88:025501, Aug 2013.
- 1119 [20] Howard Georgi and S. L. Glashow. Unity of all elementary-particle forces. *Phys. Rev.*
1120 *Lett.*, 32:438–441, Feb 1974.
- 1121 [21] Gerard Jungman, Marc Kamionkowski, and Kim Griest. Supersymmetric dark matter.
1122 *Physics Reports*, 267(5):195–373, March 1996.
- 1123 [22] The ATLAS Collaboration. Observation of a new particle in the search for the Standard
1124 Model Higgs boson with the ATLAS detector at the LHC. *Physics Letters B*, 716(1):1–
1125 29, September 2012. arXiv: 1207.7214.

- 1126 [23] The CMS Collaboration. Observation of a new boson at a mass of 125 GeV with the
1127 CMS experiment at the LHC. *Physics Letters B*, 716(1):30–61, September 2012. arXiv:
1128 1207.7235.
- 1129 [24] Standard Model Summary Plots June 2021.
- 1130 [25] Luca Lista. *Statistical Methods for Data Analysis in Particle Physics*, volume 941 of
1131 *Lecture Notes in Physics*. Springer International Publishing, Cham, 2017.
- 1132 [26] The ALICE Collaboration. The ALICE experiment at the CERN LHC. *JOURNAL OF
1133 INSTRUMENTATION*, 3, AUG 2008.
- 1134 [27] ATLAS luminosity public results run-1, March 2011.
- 1135 [28] ATLAS luminosity public results run-2, July 2015.
- 1136 [29] The European Strategy for Particle Physics. Technical Report CERN/2685, CERN,
1137 2006. Adopted by the CERN council at a special session at ministerial level in Lisbon
1138 in 2006.
- 1139 [30] HiLumi HL-LHC Project. LHC/HL-LHC plan (last update january 2021). <https://hilumilhc.web.cern.ch/content/hl-lhc-project>, last accessed on 2021-09-09.
- 1141 [31] M. Cepeda et al. Report from Working Group 2: Higgs Physics at the HL-LHC and
1142 HE-LHC. *CERN Yellow Rep. Monogr.*, 7:221–584. 364 p, Dec 2018.
- 1143 [32] ATLAS inner detector : Technical Design Report, 1. Technical Report CERN-LHCC-
1144 97-016, CERN, 1997. ISBN: 9789290831020 Publication Title: CERN Document Server.
- 1145 [33] L. Rossi, S. Haywood, A. Romanouk, and R. Nickerson. ATLAS inner detector : Tech-
1146 nical Design Report, 2. Technical Report CERN-LHCC-97-017, CERN, 1997. ISBN:
1147 9789290831037 Publication Title: CERN Document Server.
- 1148 [34] ATLAS liquid-argon calorimeter : Technical Design Report. Technical Report CERN-
1149 LHCC-96-041, CERN, 1996. ISBN: 9789290830900 Publication Title: CERN Document
1150 Server.
- 1151 [35] ATLAS tile calorimeter : Technical Design Report. Technical Report CERN-LHCC-96-
1152 042, CERN, 1996. ISBN: 9789290830917 Publication Title: CERN Document Server.
- 1153 [36] ATLAS level-1 trigger : Technical Design Report. Technical Report CERN-LHCC-98-
1154 014, CERN, 1998. ISBN: 9789290831280 Publication Title: CERN Document Server.

- 1155 [37] Technical Design Report for the Phase-II Upgrade of the ATLAS TDAQ System. Technical report, CERN, Geneva, Sep 2017.
- 1156
- 1157 [38] Marzio Nessi, Markus Nordberg, Peter Jenni, and Kenway Smith. ATLAS high-level trigger, data-acquisition and controls : Technical Design Report. Technical Report CERN-LHCC-2003-022, CERN, 2003. Publication Title: CERN Document Server.
- 1158
- 1159
- 1160 [39] A Ruiz Martínez and. The run-2 ATLAS trigger system. *Journal of Physics: Conference Series*, 762:012003, oct 2016.
- 1161
- 1162 [40] ATLAS magnet system : Technical Design Report, 1. Technical Report CERN-LHCC-97-018, CERN, 1997. ISBN: 9789290831044 Publication Title: CERN Document Server.
- 1163
- 1164 [41] ATLAS Collaboration. Performance of the ATLAS muon trigger in pp collisions at $\sqrt{s}=8\text{ TeV}$. *The European Physical Journal C*, 75(3):120, March 2015. arXiv: 1408.3179.
- 1165
- 1166
- 1167 [42] ATLAS Collaboration. ATLAS Muon Spectrometer: Technical Design Report. Technical Report CERN-LHCC-97-022, CERN, Geneva, 1997.
- 1168
- 1169 [43] S. Aefsky, C. Amelung, J. Bensinger, C. Blocker, A. Dushkin, M. Gardner, K. Hashemi, E. Henry, B. Kaplan, P. Keselman, M. Ketchum, U. Landgraf, A. Ostapchuk, J. Rothberg, A. Schricker, N. Skvorodnev, and H. Wellenstein. The Optical Alignment System of the ATLAS Muon Spectrometer Endcaps. *Journal of Instrumentation*, 3(11):P11005–P11005, November 2008. Publisher: IOP Publishing.
- 1170
- 1171
- 1172
- 1173
- 1174 [44] John Townsend. *Electricity in gases*. Clarendon Press, Oxford, 1915.
- 1175
- 1176
- 1177 [45] S. Majewski, G. Charpak, A. Breskin, and G. Mikenberg. A thin multiwire chamber operating in the high multiplication mode. *Nuclear Instruments and Methods*, 217:265–271, 1983.
- 1178
- 1179
- 1180 [46] E. Gatti, A. Longoni, H. Okuno, and P. Semenza. Optimum geometry for strip cathodes or grids in MWPC for avalanche localization along the anode wires. *Nuclear Instruments and Methods*, 163(1):83–92, July 1979.
- 1181
- 1182
- 1183 [47] G. Battistoni, P. Campana, V. Chiarella, U. Dotti, E. Iarocci, and G. Nicoletti. Resistive cathode transparency. *Nuclear Instruments and Methods in Physics Research*, 202(3):459–464, November 1982.
- 1184
- 1185 [48] P. K. F. Grieder. *Cosmic rays at Earth: researcher's reference manual and data book*. Elsevier Science Ltd, Amsterdam, 1st ed edition, 2001.

- 1186 [49] Benoit Lefebvre. *Characterization studies of small-strip Thin Gap Chambers for the*
 1187 *ATLAS Upgrade*. PhD Dissertation, McGill University, Montreal, Canada, 2018.
- 1188 [50] R. Keyes, K.A. Johnson, L. Pepin, F. Léger, C. Qin, S. Webster, A. Robichaud-
 1189 Véronneau, C. Bélanger-Champagne, B. Lefebvre, S.H. Robertson, A. Warburton,
 1190 B. Vachon, and F. Corriveau. Development and characterization of a gas system and
 1191 its associated slow-control system for an ATLAS small-strip thin gap chamber testing
 1192 facility. *Journal of Instrumentation*, 12(04):P04027–P04027, April 2017.
- 1193 [51] George Iakovidis. VMM3, an ASIC for Micropattern Detectors. In *Proceedings of*
 1194 *Science*, page 5, Philadelphia, 2017.
- 1195 [52] Bohan Chen. *Calibration Studies of the Front-End Electronics for the ATLAS New*
 1196 *Small Wheel Project*. PhD thesis, McGill University, Montreal, Canada, 2019.
- 1197 [53] R. Brun and F. Rademakers. ROOT: An object oriented data analysis framework.
Nucl. Instrum. Meth. A, 389:81–86, 1997. See also "ROOT" [software], Release 6.18/02,
 1198 23/08/2019, (<https://zenodo.org/record/3895860#.YVJW6n0pCHs>).
- 1200 [54] Fabio Sauli. Principles of operation of multiwire proportional and drift chambers. In
Cern Yellow Reports: Monographs, page 92 p, Geneva, 1977. CERN, CERN. CERN,
 1201 Geneva, 1975 - 1976.
- 1203 [55] M. Hatlo, F. James, P. Mato, L. Moneta, M. Winkler, and A. Zsenei. Developments
 1204 of mathematical software libraries for the LHC experiments. *IEEE Trans. Nucl. Sci.*,
 1205 52:2818–2822, 2005.
- 1206 [56] Hongwei Guo. A Simple Algorithm for Fitting a Gaussian Function [DSP Tips and
 1207 Tricks]. *IEEE Signal Processing Magazine*, 28(5):134–137, September 2011.
- 1208 [57] Xiao Zhao, Wenlong Li, Dengfeng Zhang, Changyu Li, Han Li, Shengquan Liu, Peng
 1209 Miao, Yanyan Du, Yanyun Duan, and Chengguang Zhu. Cosmic test of sTGC detector
 1210 prototype made in China for ATLAS experiment upgrade. *Nuclear Instruments and Methods in Physics Research Section A: Accelerators, Spectrometers, Detectors and*
 1211 *Associated Equipment*, 927:257–261, May 2019.
- 1213 [58] Ichita Endo, Tatsuo Kawamoto, Yoshinari Mizuno, Takashi Ohsugi, Takashi Taniguchi,
 1214 and Tohru Takeshita. Systematic shifts of evaluated charge centroid for the cathode
 1215 read-out multiwire proportional chamber. *Nuclear Instruments and Methods in Physics*
 1216 *Research*, 188(1):51–58, September 1981.

- 1217 [59] Bernd Stelzer. The New Small Wheel Upgrade Project of the ATLAS Experiment.
1218 *Nuclear and Particle Physics Proceedings*, 273-275:1160–1165, April 2016.
- 1219 [60] Manfred Krammer. Upgrade Programs of the LHC Experiment, November 2017.
- 1220 [61] Benoit Lefebvre. stgc_as_built_fit.
- 1221 [62] Benoit Lefebvre. tgc_analysis.
- 1222 [63] The ATLAS Collaboration. Athena.
- 1223 [64] Lia Formenti. cosmics_xray_correlation.
- 1224 [65] Siyuan Sun. sTGC_readout_sw.
- 1225 [66] G Brianti. Large Hadron Collider in the LEP Tunnel. In *Proceedings of the ECFA-CERN*
1226 *Workshop*, volume 1, page 352, Lausanne and Geneva, March 1984.
- 1227 [67] Letter of Intent for the Phase-I Upgrade of the ATLAS Experiment. Technical Report
1228 CERN-LHCC-2011-012. LHCC-I-020, CERN, Geneva, November 2011.
- 1229 [68] ATLAS: letter of intent for a general-purpose pp experiment at the large hadron collider
1230 at CERN. Technical Report CERN-LHCC-92-004, CERN, Geneva, 1992.
- 1231 [69] The ATLAS Collaboration. Technical Design Report for the Phase-I Upgrade of the
1232 ATLAS TDAQ System. Technical report, Sep 2013. Final version presented to December
1233 2013 LHCC.

1234 APPENDICES

1235 **Appendix A**

1236 **Uncertainty in cluster positions**

1237 **A.1 Cluster definition**

1238 A cluster is a series of contiguous strip channels on a layer with non-zero amplitude, all
1239 part of the same trigger and having the same event number [49]. Clusters result from the
1240 drift of ionization products generate in the ionization avalanche caused by a muon [44]. The
1241 peak-detector-output (PDO) of the signal on each strip of a cluster is fit with a Gaussian.
1242 The y-position of a particle as it passed through the layer is mean of the cluster, referred to
1243 here as the hit position.

1244 **A.2 Effect of fit algorithm on cluster mean**

1245 The clusters were fit with Guo's method [56] and Minuit2 for ROOT [55]. The difference in
1246 cluster means between the two algorithms is shown in figure A.1.

1247 The RMS of the distribution in figure A.1 is 57 μm , which is much larger than the statistical
1248 uncertainty in the mean for the Minuit2 algorithm, which peaks around 7 μm . An RMS of
1249 60 μm is common for data taken with most quadruplets at 3.1 kV. Therefore, the uncertainty
1250 in the y-hit positions is assigned 60 μm .

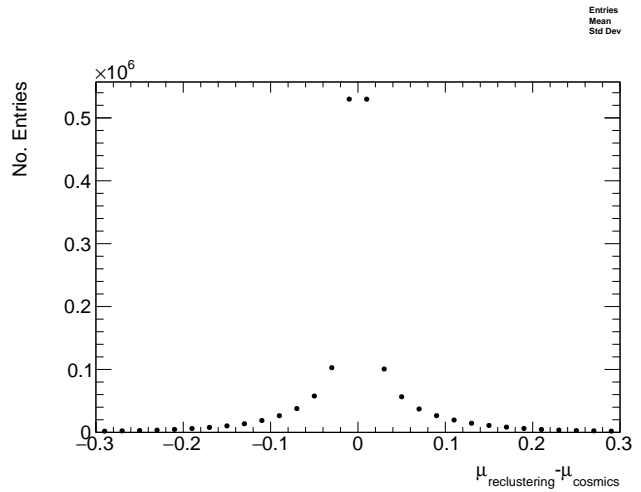


Figure A.1: The difference between cluster means calculated with Guo's method [56] in `tgc_analysis/CosmicsAnalysis` and `Minuit2` for `ROOT` [55] in `strip_position_analysis/ReClustering` for data collected with QL2.P.8 at 3.1 kV.

1251 **A.3 Effect of uncertainty in cluster mean on track residuals**

1252

1253 The uncertainty assigned to the hit position affected the uncertainty in the extrapolated/interpolated
1254 position of the track, and in the residuals. The bin size of the residual distributions was set
1255 to 200 μm because that was the uncertainty in the residuals calculated from the tracks with
1256 the least favourable geometry (like tracks built from hits on layers 1 and 2 and extrapolated
1257 to layer 4).

1258 **Appendix B**

1259 **Study of cosmics for alignment
1260 analysis statistical uncertainty**

1261 Typically, one million triggers (cosmic muon events, noise, photons and δ -rays) were collected
1262 for each Canadian quadruplet at McGill University, resulting in roughly half the number of
1263 viable tracks after cuts. For QS3.P.18, 3.5 million triggers were collected. To gauge the
1264 sensitivity of the analysis to the available statistics, partitions of this data with each with
1265 a different number of triggers were analyzed separately. Ultimately, the quantity of interest
1266 was the gaussian mean of the residual distribution in regions of interest, so the peak in the
1267 distribution of the statistical uncertainty in the residual means for each area of interest for
1268 a specific tracking combination was used to gauge the quality of the analysis. How the peak
1269 in the residual mean uncertainty distribution changes with the number of triggers is shown
1270 in figure for tracks on layer 1 built from layers 3 and 4 [B.1](#).

1271 The uncertainty is already around 20 μm at 1 million triggers, suitable for distinguishing
1272 differences in offsets of order 50 μm as required. Although increased statistics could decrease
1273 the statistical uncertainty, it is not required for the goals of this analysis. Moreoever, the
1274 systematic uncertainty is around 50 μm and the systematic uncertainty on the x-ray residuals
1275 is 150 μm so the statistical uncertainty of 20 μm is nearly negligible.

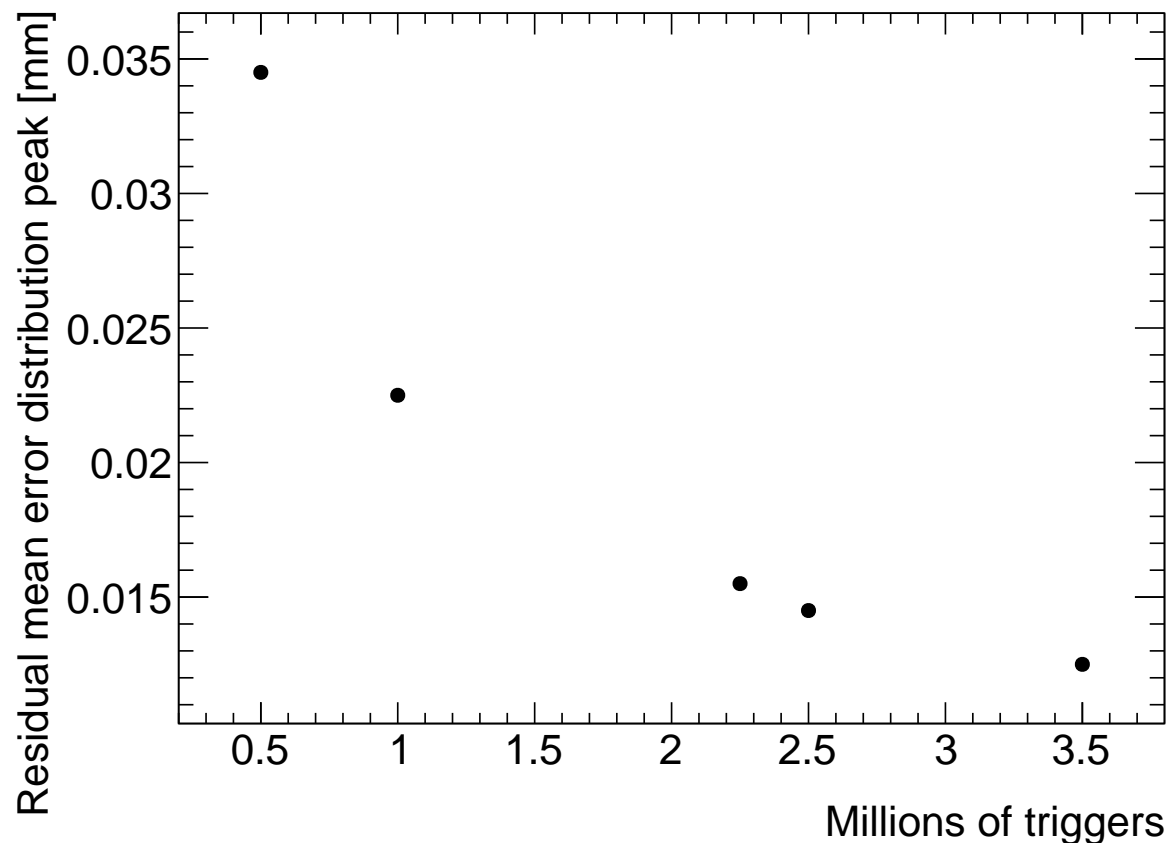


Figure B.1: How the peak of the distributions of uncertainties in the residual means in regions of interest for tracks on layer 1 built from layers 3 and 4 changed with the number of triggers used in the analysis. The distribution falls off as $\frac{1}{\sqrt{N}}$ as expected.

1276 Appendix C

1277 Study of systematic uncertainties 1278 when using cosmics data for 1279 alignment studies

1280 C.1 Residual distribution fit function

1281 The distribution of residuals should be modelled by a double gaussian fit[49]:

$$G(r) = A_s \exp \left[\frac{-(r - \mu)^2}{2\sigma_s^2} \right] + A_b \exp \left[\frac{-(r - \mu)^2}{2\sigma_b^2} \right] \quad (\text{C.1})$$

1282 where r is the residual, A is the gaussian amplitude, μ is the gaussian mean, σ is the
1283 gaussian sigma, and the subscripts s and b stand for signal and background respectively.
1284 One gaussian captures the real (signal) tracks and the other captures the tracks built from
1285 noise (background). The gaussian with the smaller width is identified as the signal.

1286 A single gaussian fit failed less often than a double gaussian fit. The gaussian fits were
1287 performed by initially estimating the amplitude to be 100 tracks, the gaussian mean to be
1288 the histogram mean, and gaussian σ to be the RMS. The fit range was restricted to ± 1 RMS
1289 from the histogram mean. The modification helped the gaussian fit capture the signal peak.
1290 An example residual distribution is shown in figure C.1.

1291 For all residual distributions in 100 mm by 100 mm bins on layer 4 built from hits on layers 1
1292 and 2, the difference in gaussian and double gaussian means and σ 's is shown in figure C.2.
1293 Since the RMS of the residual mean differences distribution is less than 50 μm the gaussian

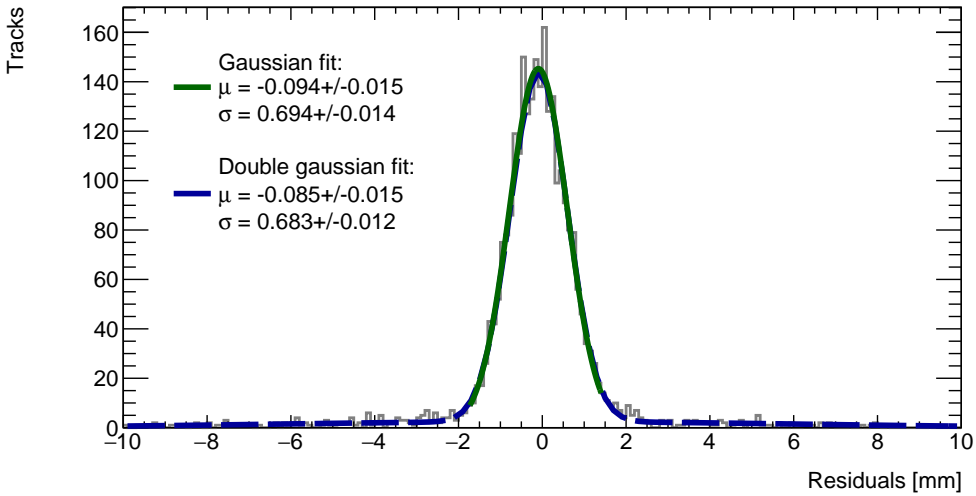


Figure C.1: Residual distribution for tracks on layer 4 built from hits on layers 1 and 2 for $x \in [-3.00, 97.00]$, $y \in [394.60, 494.60]$ mm for QL2.P.8 fit with a double gaussian and a single gaussian in a range of ± 1 RMS from the histogram mean.

1294 fit gave the same result within the required precision. Moreover, this is for the tracking
1295 combination with the worst extrapolation lever arm and the widest distribution of mean
1296 differences; the interpolation combinations have narrower distributions.

1297 The gaussian σ should be larger than the double gaussian σ because the gaussian distribution
1298 includes the effect of the noise tracks with large residuals, while the double gaussian models
1299 signal and background residuals separately. For this analysis, only the residual mean was
1300 important, so the systematic overestimate of the signal σ in the gaussian fit shown on the
1301 right of figure C.2 was allowed.

1302 C.2 Cosmic muon data collection voltage

1303 Cosmic muon data was collected at 2.9 kV and 3.1 kV because although 2.9 kV is closer to
1304 the operating conditions the chambers will be subject to in ATLAS, the extra gain provided
1305 by operating at 3.1 kV increased the signal to noise ratio for pad signals. Also, the tracking
1306 efficiency was higher with data collected at 3.1 kV. The difference in gain affected the relative
1307 population of clusters of different sizes, which in turn affected the uncertainty in the strip hit
1308 positions on each layer, the uncertainty in the track positions and the residual distributions.
1309 The residual distributions for 3.1 kV data are narrower, as shown in figure C.3.

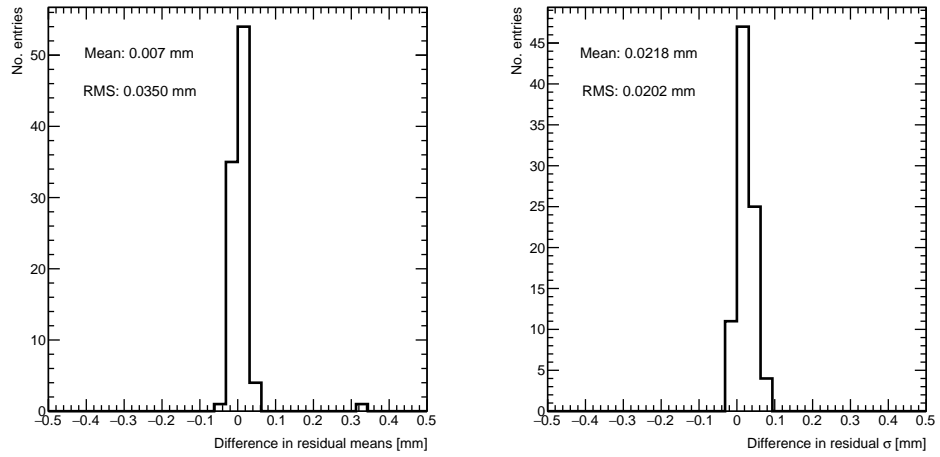


Figure C.2: Difference in residual distribution means and σ 's for a gaussian and double gaussian fit, for all residual distributions in 100 mm by 100 mm bins on layer 4 built from hits on layers 1 and 2 for QL2.P.8.

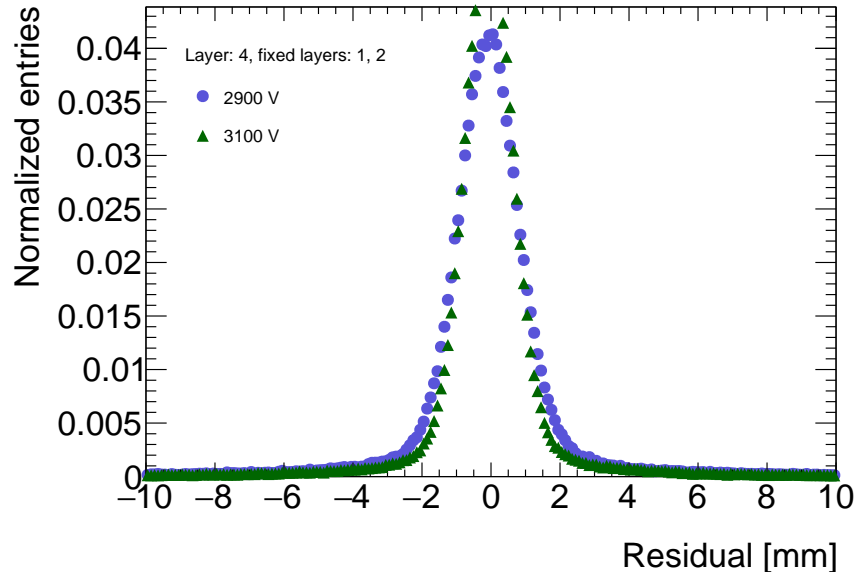


Figure C.3: Residual distribution for tracks on layer 4 built from hits on layers 1 and 2 for QL2.P.8 for data collected at 2.9 kV and 3.1 kV.

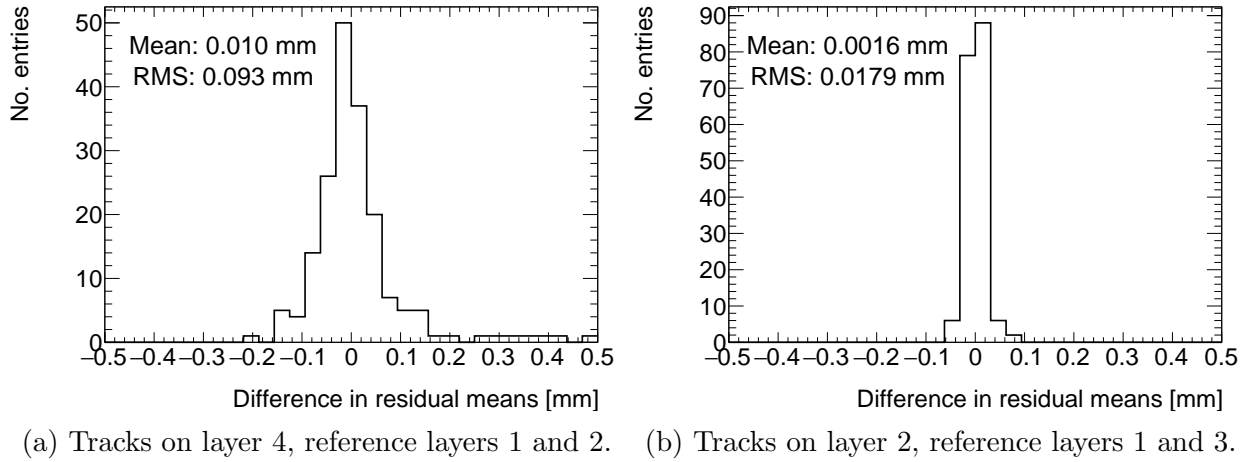


Figure C.4: Difference in residual means for data collected with QL2.P.8 at 2.9 kV and 3.1 kV respectively in 100 mm by 100 mm bins for (a) tracks on layer 4 built from hits on layers 1 and 2 and (b) tracks on layer 2 built from hits on layers 1 and 3.

1310 Neither dataset is better for calculating the mean of residuals in a given area, so a systematic
 1311 uncertainty can be assigned based on the difference in residual means calculated for 2.9 kV
 1312 and 3.1 kV data; namely, the systematic uncertainty was approximated as the RMS of the
 1313 residual mean difference distribution. Data taken with QL2.P.8 was used to estimate the
 1314 RMS, as in figure C.4a.

1315 Tracks built from hits on layers 1 and 2 and extrapolated to layer 4 have the worst lever arm
 1316 and hence the most uncertainty. The width of the distribution for geometrically favourable
 1317 tracks are much narrower. The narrowest width of the residual mean difference distribution
 1318 is for tracks on layer 2 built from hits on layers 1 and 3 (see figure C.4b).

1319 Therefore, for each tracking combination, a systematic uncertainty equal to the RMS of the
 1320 residual mean difference distribution was assigned.

1321 C.3 Cluster fit algorithm

1322 To ensure that changing the cluster fitting algorithm like in appendix A would not change
 1323 the calculated mean of residuals in each region of interest significantly, the residual means
 1324 were compared in both cases. The distribution of the difference in residual means is plotted
 1325 in figure C.5 for the tracking combination with the worst extrapolation lever arm.

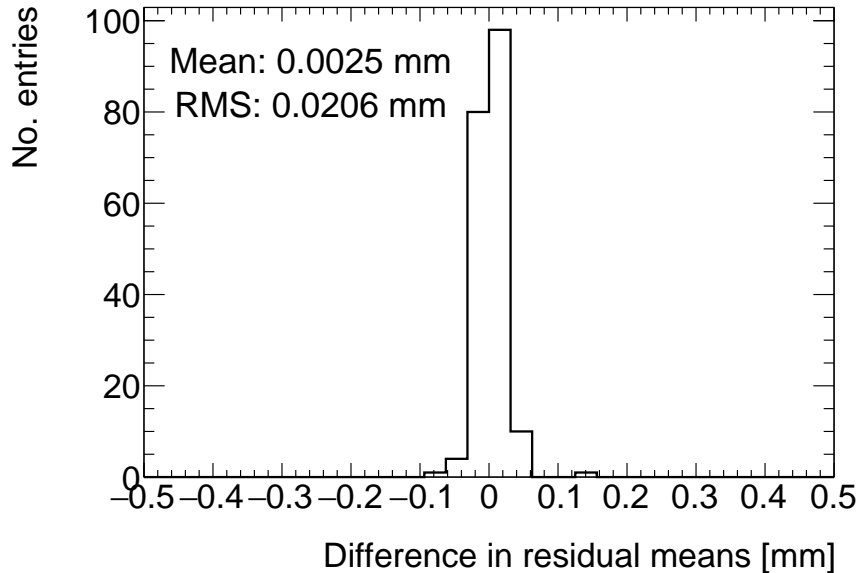


Figure C.5: Difference in residual means when the cluster fit algorithm is `Minuit2` [55] versus Guo’s method [56] for tracks on layer 4 built from hits on layers 1 and 2 for QL2.P.8.

1326 The other tracking combinations had smaller RMS values. Differences on the order of 50 μm
 1327 are important, so figure C.5 shows that the clustering algorithm had a small but notable
 1328 effect. Therefore, the RMS for each tracking combination will be used to add a systematic
 1329 uncertainty on the residual means.

1330 C.4 Differential non-linearity

1331 Definition

1332 In this context, differential non-linearity (DNL) is when the reconstructed cluster mean is
 1333 biased by the fit of the discretely sampled PDO distribution over the strips. The bias depends
 1334 on the relative position of the avalanche with respect to the center of the closest strip. For a
 1335 summary of DNL, refer to page 40 of Lefebvre’s thesis [49] and for an example application,
 1336 refer to [6].

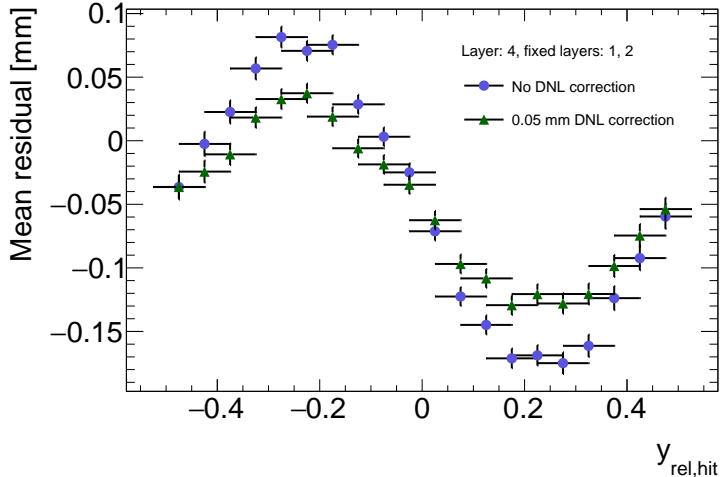


Figure C.6: Effect applying a 50 μm DNL correction to the cluster means on the residual vs y_{rel} distribution for tracks built from layers 1 and 2 and extrapolated to layer 4 for QL2.P.8.

1337 **Application and effect of DNL**

1338 The cluster mean was corrected for DNL using the equation:

$$y' = y + a \sin(2\pi y_{rel}) \quad (\text{C.2})$$

1339 where y is the cluster mean, y_{rel} is the relative position of the cluster mean with respect to
1340 the strip's center, a is the amplitude of the correction, and y' is the corrected cluster mean.
1341 The amplitude can be derived by comparing the reconstructed hit position to the expected
1342 hit position, as done in Abusleme, 2016 [6]. With cosmic muons, there is no reference hit
1343 position to compare to, so track residuals were used as a proxy [49]. The hallmark of the DNL
1344 effect is the periodic pattern in the residual versus y_{rel} profile, and the effect of correcting
1345 the cluster means using an amplitude of 50 μm is shown in figure C.6. An amplitude of
1346 50 μm was based on Lefebvre's estimate of the DNL amplitudes by layer, quadruplet and
1347 cluster size using exclusive cosmic muon tracks in `tgc_analysis/CosmicsAnalysis`. Little
1348 variation was seen in the amplitude parameters with respect to the quadruplet tested, the
1349 layer and the cluster size so a universal correction was used.

1350 Although the correction is not large enough in this case, the figure shows that the correction
1351 does reduce the DNL effect. Slightly better performance is seen in the interpolation tracking
1352 combinations where the quality of the residuals is better. DNL corrections for cosmic muon
1353 data are difficult because the DNL effect is obscured by the effect of misalignments and

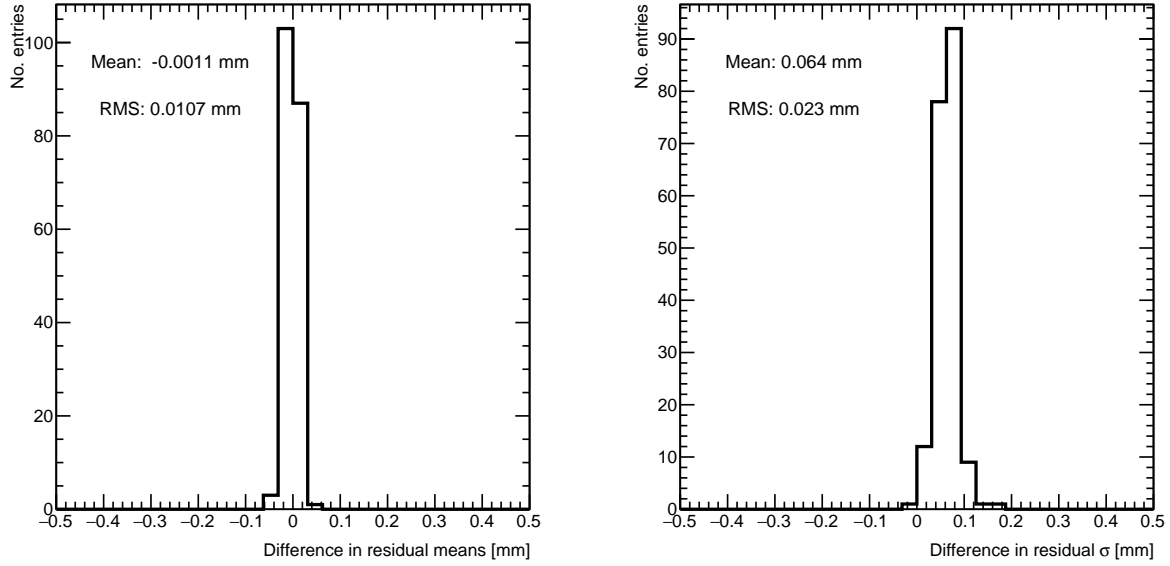


Figure C.7: Difference in residual distribution means and σ 's with and without DNL correction for residuals on layer 4 from reference layers 1 and 2 for QL2.P.8.

1354 noise. Misalignments cause the center of the sine pattern in figure C.6 to be shifted off of
 1355 zero, since the mean of residuals is shifted.

1356 In figure C.7, it is apparent that the effect of the DNL correction on the mean of the
 1357 residual distribution in 100 mm by 100 mm areas is on the order of micrometers in the worst
 1358 extrapolation case. Although the σ 's of the residual distributions shrink with the DNL
 1359 correction, the mean is the parameter of interest. Therefore, for this analysis DNL was not
 1360 corrected for.

1361 The σ 's of the residual distributions do shrink with the DNL correction but not so much to
 1362 affect the residual means, which are the important parameter for this analysis. Therefore,
 1363 since the effect of the DNL correction is negligible, it was not pursued further.

₁₃₆₄ Appendix D

₁₃₆₅ Printable plots

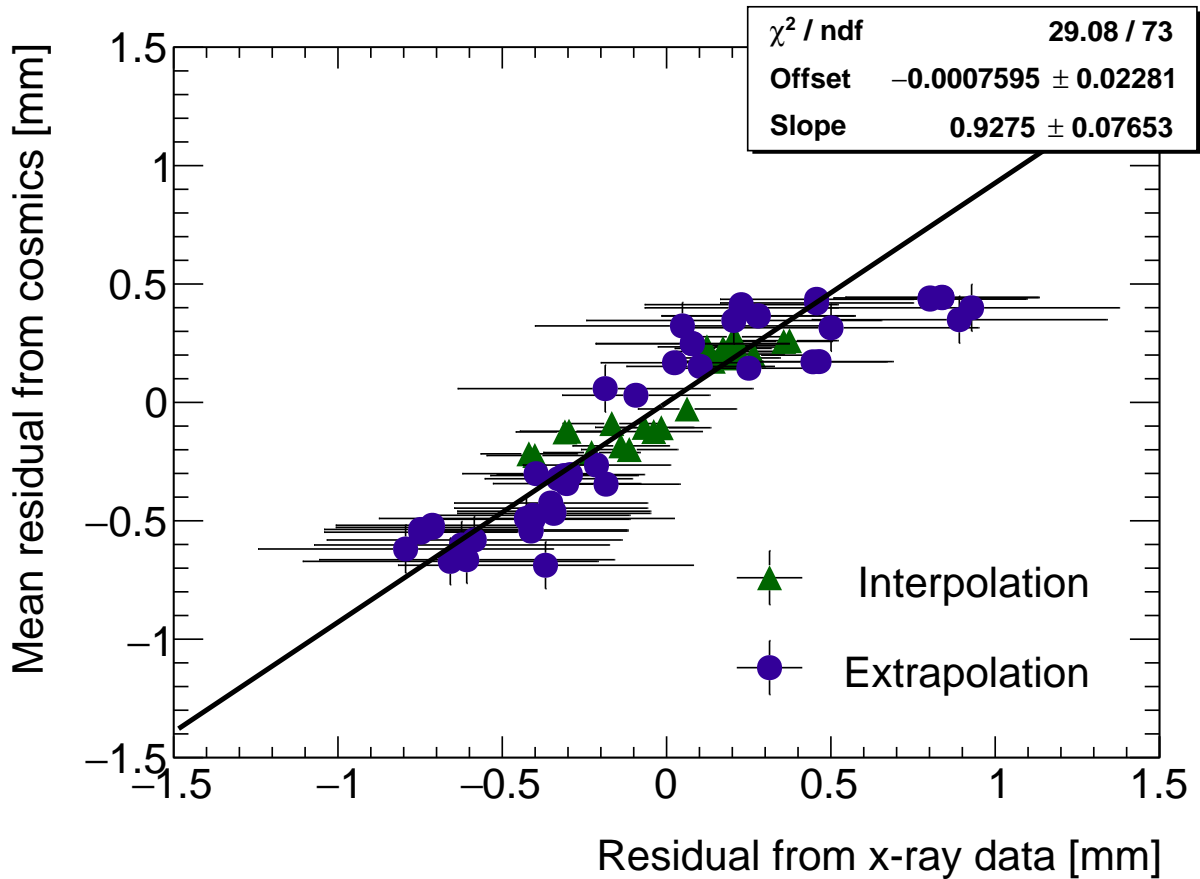


Figure D.1: Correlation plot between x-ray and cosmics residuals for all tracking combinations for QL2.P.11. Each rectangle is centered on an x-ray and mean cosmics residual pair. The width of the rectangles in x and y are the uncertainty in the x-ray and mean cosmics residual respectively. This is a printable version of figure 6.2 in section 6.1.

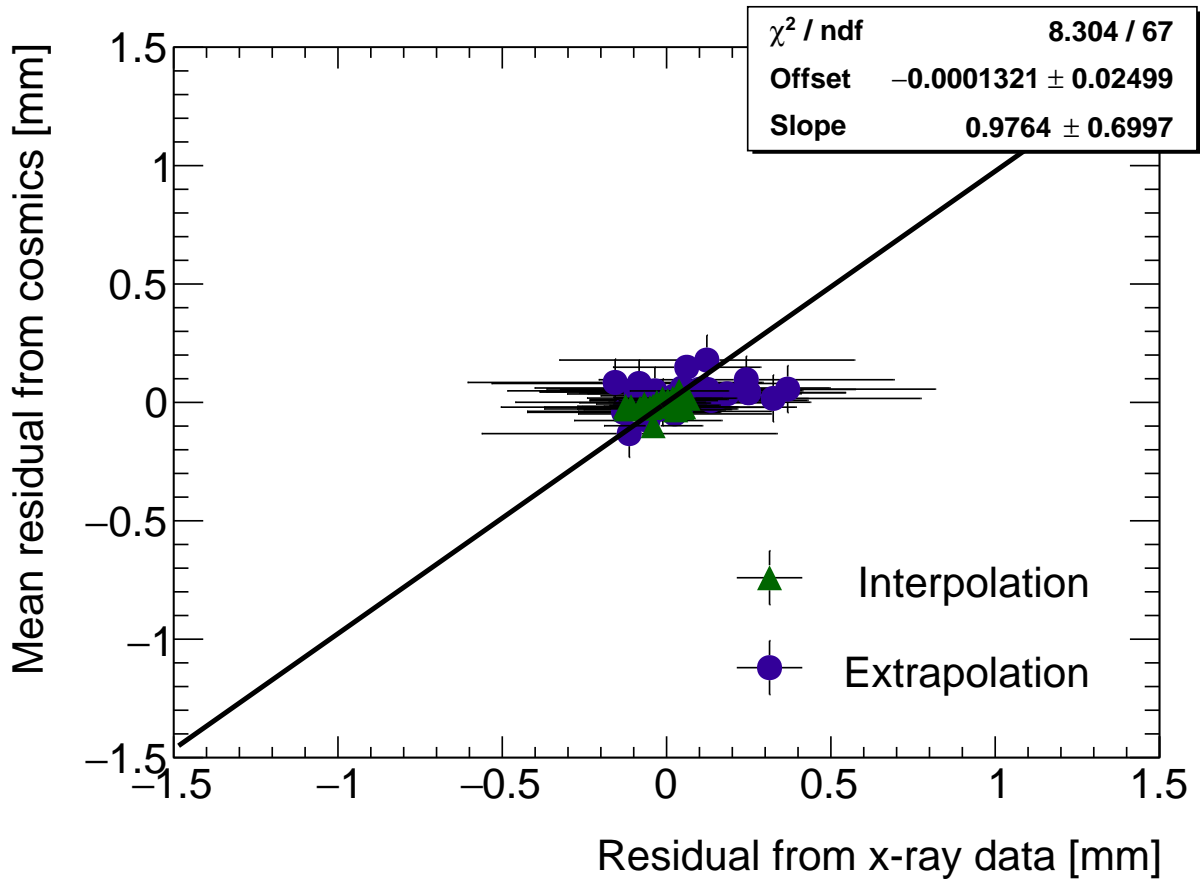


Figure D.2: Correlation plot between x-ray and cosmics residuals for all tracking combinations for QL2.P.8. Each rectangle is centered on an x-ray and mean cosmics residual pair. The width of the rectangles in x and y are the uncertainty in the x-ray and mean cosmics residual respectively. This is a printable version of figure 6.3 in section 6.1.